Article

Radial Dual Lattice Graphs via Admissible Inversion: Exact Folding Operators for Eisenstein, Hurwitz, and E_8 Lattices — A Clifford-Algebraic Cl(8) Formulation

Nathan O. Schmidt *, Klee Irwin, Natasha Urakhchina

Posted Date: 1 June 2026

doi: 10.20944/preprints202605.2108.v1

Keywords: hyperspherical inversion; lattice graph isomorphism; sphere packing; root systems; Clifford algebra; octonions; quasicrystals; Cycle Clock Theory; exact arithmetic; shell enumeration; divisor sums; H4 folding; 600-cell; quantum gravity

 doi:10.20944/preprints202605.2108.v1

Article

Radial Dual Lattice Graphs via Admissible Inversion: Exact Folding Operators for Eisenstein, Hurwitz, and E_8 Lattices—A Clifford-Algebraic Cl(8) Formulation

Nathan O. Schmidt [1,*], Klee Irwin [2] and Natasha Urakhchina [2]

[1] Cold Hammer Research & Development LLC, Eagle, Idaho, USA
[2] Quantum Gravity Research, Topanga, California, USA
* Correspondence: nate.o.schmidt@coldhammer.net

Abstract

We construct radial dual lattice graphs for the Eisenstein, Hurwitz, and E_8 lattices using admissible hyperspherical inversion. The inversion induces exact bijections between outer zone vertices and rational inner zone representatives, and it gives transported-edge graph isomorphisms once the radial-dual edge relation is defined. We verify the norm relation, involution, shell compression, and finite-shell adjacency identities using exact arithmetic. Composing the radial inversion with the Moxness E_8-to-H_4 folding matrix $H_{4\text{fold}}$ gives a candidate golden linear-radial dual compressor Y_r for Cycle Clock Theory (CCT) workflows; on the E_8 root shell, the top 4×8 projection block Π of $H_{4\text{fold}}$ maps the 240 roots into two 120-point layers (the regular 600-cell H_4 and its golden-ratio scaled copy $H_4\Phi$, with radius ratio Φ, equivalently squared-norm ratio Φ^2). For larger shells, this compressor is validated on finite domains and proposed as a proof target for full cycle-clock enumeration. The framework aligns naturally with the classical divisor-sum expression $c_8(n) = 240\,\sigma_3(n)$ for E_8 shell multiplicities and makes it computationally useful for folded inner zone enumeration: our benchmark reports 83 000–260 000$\times$ speedups over exact-arithmetic Jacobi theta polynomial expansion at moderate shell indices. Realized via the Cayley integers in 8D, the construction aligns conceptually with octonion-based models in quasicrystalline quantum gravity while remaining strictly algebraic and geometric, operating on rational extensions without approximations, floating-point drift, continuous relaxations, or information loss. The construction offers a practical exact-arithmetic method for shelling and scaling calculations, while full global injectivity of Y_r on L^8, 8D-to-4D graph-isomorphism preservation across arbitrary shells, and end-to-end CCT simulation integration remain proof obligations for future work. The entire construction is formulated inside the real Clifford algebra $\mathrm{Cl}(8)$ as the enveloping associative algebra: A_2, D_4, and E_8 are realized as the grade-1 root sub-systems of $\mathrm{Cl}(2)$, $\mathrm{Cl}(4)$, and $\mathrm{Cl}(8)$ respectively, and the classical Eisenstein, Hurwitz, and Cayley integer rings are recovered as the even subalgebras $\mathrm{Cl}^+(d)$ acting on these generators. Under this enveloping algebra we adopt the uniform packing-radius root-length convention $\langle \alpha, \alpha \rangle = 2$ (Euclidean length $\sqrt{2}$) across all three lattices, in agreement with the Bourbaki/Conway–Sloane/Viazovska normalization and with the maximally dense sphere-packing radius in each dimension; the canonical admissible inversion radius is therefore $r = \sqrt{2}$ uniformly, and the hyperspherical inversion ι_r is Clifford-equivariant under $\mathrm{Pin}(d) \subset \mathrm{Cl}(d)$.

Keywords: hyperspherical inversion; lattice graph isomorphism; sphere packing; root systems; Clifford algebra; octonions; quasicrystals; Cycle Clock Theory; exact arithmetic; shell enumeration; divisor sums; H4 folding; 600-cell; quantum gravity

1. Introduction

The exceptional lattices associated with the normed division algebras stand in a unique and structurally inevitable position in mathematics, computer science, and theoretical physics. These

 doi:10.20944/preprints202605.2108.v1

structures emerge directly from the geometry of maximally dense sphere packings [1,2] in 1D, 2D, 4D, and 8D—the only dimensions that admit such algebras—which render the construction rigid and canonical instead of arbitrary.

This finite exceptional set of specific dimensional levels—which fundamentally terminates at 8D by the Hopf invariant one theorem of Adams [3]—is precisely what facilitates the admissibility condition for inversion radii with its profound mathematical significance, while ensuring that the discrete symmetry-invariant shells enable exact bijective radial dualities (in the transported-edge sense) throughout the recursive bootstrapping process.

This first principles work generalizes the Eisenstein integer based Tri-Quarter Framework (TQF) [4] from 2D to 4D and 8D within the Clifford-algebraic enveloping algebra $\mathrm{Cl}(8)$, under which A_2, D_4, and E_8 arise as the grade-1 root sub-systems of $\mathrm{Cl}(2)$, $\mathrm{Cl}(4)$, and $\mathrm{Cl}(8)$ respectively and share a single uniform root-length normalization $\langle \alpha, \alpha \rangle = 2$, without sacrificing the exact discrete, rational, and efficient character of the original. We design and deploy *radial dual lattice graphs* by driving admissible hyperspherical inversion straight through the nearest-neighbor graph of each exceptional lattice.

Hyperspherical inversion denotes the classical geometric transformation that inverts points with respect to a hypersphere of radius r centered at the origin in $\mathbb{R}^n$. It is the direct higher-dimensional generalization of circular inversion in the plane and spherical inversion in 3D. Although these inversions have a long history in geometry—tracing to foundational contributions by Jakob Steiner in 1824 and systematically developed in the theory of inversive geometry [5,6]—their specific application here to admissible radii determined by the norm form of exceptional lattices is novel. This application, which induces transported-edge graph isomorphisms between the outer zone and inner zone subgraphs of the radial dual lattice graph, begins from the original 2D radial dual graph construction [4].

The present framework is distinguished by its purely algebraic and geometric nature, while operating exclusively on rational extensions of the underlying exceptional lattices—with no approximations, floating-point drift, continuous relaxations, or information loss. The construction remains entirely within rational extensions of the lattices—this uncompromising exactness is its core advantage.

At each dimensional level of exception, the inversion map induces a transported-edge graph isomorphism that preserves the transported adjacency relation, the norms of pre-images, the radial directions of vertices, and the action of the relevant symmetry groups. For instance, as we demonstrate in this paper, the 8D radial dual equips Cycle Clock Theory (CCT) with an exact radial-folding operator that maps outer zone cycle clocks on the E_8 lattice to compact inner zone equivalents in the rational extension. This reduces computational complexity in the simulation and enumeration of quasicrystalline dynamics while preserving combinatorial invariants in the transported sense. In this context, the present construction constitutes a direct algebraic assault on what is a great challenge of E_8-based modeling: the explosive growth in combinatorial scale and computational intractability encountered when simulating or enumerating quasicrystalline dynamics and cycle clocks at large radial norms on the E_8 lattice. The radial dual framework directly addresses this challenge by providing an exact reversible coordinate-compression and folding mechanism. In particular, the framework aligns naturally with the classical divisor-sum expression $c_8(n) = 240\,\sigma_3(n)$ for E_8 shell multiplicities (the weight-4 Eisenstein series identity for the E_8 theta function [19]), making this identity computationally useful for folded inner zone enumeration: our benchmark shows speedups of more than $80\,000\times$ at shell index $n = 1\,000$ and over $260\,000\times$ at $n = 2\,000$, with the advantage continuing to scale favorably for increasingly large shell indices. The golden linear-radial dual compressor Υ_r, constructed by composing the Moxness E_8-to-H_4 matrix $H_{4\mathrm{fold}}$ [7] with radial dual admissible hyperspherical inversion, maps the 240 roots of L^8 onto two 120-point 600-cell layers (H_4 and its golden-ratio scaled copy $H_4\Phi$, radius ratio Φ, squared-norm ratio Φ^2) and provides a candidate dimensional-reduction operator for larger finite domains of CCT relevance. The framework aligns directly with octonion-based models through a realization via the Cayley integers (integral octonions) in 8D.

 doi:10.20944/preprints202605.2108.v1

Evidence tiers.

Throughout this paper we distinguish four kinds of claim, and the reader is invited to keep them separate:

- *[By construction]* statements about the transported-edge radial-dual graph structure: inner zone edges are defined as images of outer zone nearest-neighbor edges under ι_r, so the transported-edge graph isomorphisms of Theorems 1, 2, and 3 are immediate once the edge relation is fixed.
- *[Algebraic]* identities that follow from elementary properties of ι_r on $\mathbb{R}^d \setminus \{0\}$: the involution property, the norm relation $N(\iota_r(\mathbf{x})) = r^4/N(\mathbf{x})$, the angular preservation, the zone-swapping bijection, and the adjacency norm identity (Remark 1).
- *[Finite-shell verified]* computational facts established by exact arithmetic over $\mathbb{Q}$ or $\mathbb{Q}(\sqrt{5})$ on enumerated finite domains: the bijection of Π on the 240-root shell onto $H_4 \cup H_4\Phi$ with squared-norm ratio Φ^2 (Proposition 1), the adjacency, involution, and shell-compression verifications of Section 8, and the finite-domain FIG demonstration of Section 8.2.
- *[Future work]* claims that remain proof obligations: global injectivity-preserving graph isomorphism for the golden linear-radial dual compressor Υ_r on the full outer zone $\Lambda^8_{+,r}$, an all-shell uniform lower bound on $\|\Pi\mathbf{x}\|/\|\mathbf{x}\|$, end-to-end CCT simulation integration with phason and gauge dynamics, and the comprehensive large-scale validation of the 8D transported-edge graph isomorphism at higher norms.

While the radial dual construction, the induced transported-edge graph isomorphisms, the coordinate compression, the explicit cycle-clock folding, and the divisor-sum acceleration of shell multiplicities are rigorously established in this work at the [by construction], [algebraic], and [finite-shell verified] tiers, their comprehensive application to full CCT simulations—including large-norm cycle-clock enumeration, phason/gauge dynamics, and end-to-end projection pipelines—remains a [future work] goal.

The paper is organized as follows:

- Section 2 establishes the general notation, standing assumptions, and definitions (including admissible radii, the hyperspherical inversion map, and the transported edge relation) used throughout the work;
- Section 3 recaps the original 2D Eisenstein integer based radial dual lattice graph of the TQF [4];
- Sections 4 and 5 bootstrap the construction recursively to the 4D Hurwitz quaternion lattice and the 8D E_8 lattice to prove the corresponding transported-edge graph isomorphisms;
- Section 6 introduces the complementary linear H_4 folding operator and its composition with radial inversion, with the bijection on the 240-root shell stated as a finite-shell-verified proposition and the global-shell extension stated as a future-work proof obligation;
- Section 7 details the applications to CCT, which includes explicit cycle clock examples, connections to shelling and scaling analyses, and an embedded-root-systems subsection observing that the G_2 and F_4 root systems arise within the shell structure of A_2 and D_4;
- Section 8 reports comprehensive computational verification using exact arithmetic; and
- Section 9 concludes with implications and future directions.

With our intent and direction solidified, we proceed to drive the radial dual lattice graph construction, starting from the Eisenstein integers. But first, we introduce some generalized notation.

2. Notation and Standing Assumptions

Throughout this work we operate in Euclidean space $\mathbb{R}^d$ identified with the grade-1 generator subspace of the real Clifford algebra $\mathrm{Cl}(d)$, equipped with the squared norm $N(\cdot)$ induced by the Clifford quadratic form, for $d \in \{2, 4, 8\}$. The symbol $N(\mathbf{v})$ always denotes the *squared* Euclidean norm of $\mathbf{v}$ (so that for example $N(\mathbf{v}) = 2$ means $\|\mathbf{v}\| = \sqrt{2}$); the unsquared length is written $\|\mathbf{v}\|$ when needed. Let L^d denote the corresponding exceptional lattice realized as the grade-1 root sub-system of $\mathrm{Cl}(d)$ (the A_2 root system inside $\mathrm{Cl}(2)$ for $d = 2$, the D_4 root system inside $\mathrm{Cl}(4)$ for $d = 4$, and the

 doi:10.20944/preprints202605.2108.v1

E_8 root system inside $\mathrm{Cl}(8)$ for $d = 8$); the classical Eisenstein, Hurwitz, and Cayley integer rings are recovered as the even subalgebras $\mathrm{Cl}^+(d)$ acting by Clifford multiplication on these grade-1 generators. The punctured nearest-neighbor graph on $L^d \setminus \{0\}$ is denoted Λ^d.

Throughout this work, each element $\mathbf{v} \in L^d$ ($d = 2, 4, 8$) is understood simultaneously as

- a *lattice point* in the exceptional lattice $L^d \subset \mathbb{R}^d$,
- a *vertex* of the punctured nearest-neighbor graph Λ^d, and
- a *vector* in Euclidean space $\mathbb{R}^d$.

We adopt the convention that the generic symbols $\mathbf{v}$ and $\mathbf{u}$ (together with their primed or indexed variants $\mathbf{v}'$, $\mathbf{u_i}$, etc.) refer interchangeably to these three equivalent objects when the element lies in L^d. For points in the rational extension $\mathbb{Q} \otimes L^d$ (in particular the inner zone $\Lambda^d_{-,r}$), we retain the same symbols $\mathbf{v}$ and $\mathbf{u}$ but understand them primarily as *vertices* of the radial dual graph and as *vectors* in $\mathbb{R}^d$, while no longer referring to them as lattice points of L^d. This convention is consistent with the notational practice established in the TQF [4].

Definition 1 (Admissible inversion radius)**.** *Let $L^d \subset \mathbb{R}^d$ ($d = 2, 4, 8$) be one of the exceptional lattices equipped with the squared Euclidean norm $N(\cdot)$. A radius $r > 0$ is said to be* admissible *(with respect to L^d) if there exists a nonzero vector $\mathbf{v} \in L^d$ such that*

$$r^2 = N(\mathbf{v}).$$

For any admissible radius $r > 0$ (i.e., r^2 equals the squared norm of some nonzero lattice vector), let S_r^{d-1} denote the hypersphere of radius r centered at the (punctured) origin in $\mathbb{R}^d$. The vertex set of Λ^d is partitioned into three disjoint zones:

- **Outer zone**: $\Lambda^d_{+,r} = \{\mathbf{v} \in L^d \mid N(\mathbf{v}) > r^2\}$,
- **Boundary zone (threshold shell)**: $\Lambda^d_{T,r} = \{\mathbf{v} \in L^d \mid N(\mathbf{v}) = r^2\} = L^d \cap S_r^{d-1}$,
- **Inner zone**: $\Lambda^d_{-,r} = \iota_r(\Lambda^d_{+,r}) \subset \mathbb{Q} \otimes L^d$.

The inversion map is defined on nonzero vertices by

$$\iota_r(\mathbf{v}) = \frac{r^2\,\mathbf{v}}{N(\mathbf{v})}, \qquad \mathbf{v} \in \mathbb{R}^d \setminus \{0\}.$$

This is the direct higher-dimensional generalization of circular inversion. In all dimensions it satisfies the following algebraic properties (verified by direct substitution into the definition):

1. **Involution**: $\iota_r(\iota_r(\mathbf{v})) = \mathbf{v}$.
2. **Boundary fixed set**: If $N(\mathbf{v}) = r^2$ then $\iota_r(\mathbf{v}) = \mathbf{v}$.
3. **Zone swap**: $\iota_r(\Lambda^d_{+,r}) = \Lambda^d_{-,r}$ and vice versa.
4. **Angular preservation**: $\arg(\iota_r(\mathbf{v})) = \arg(\mathbf{v})$; each vertex and its image live on the same radial ray from the origin.
5. **Norm relation**: $N(\iota_r(\mathbf{v})) = r^4/N(\mathbf{v})$.

Remark 1 (Adjacency norm identity (general))**.** *Let $\mathbf{u}, \mathbf{v} \in \Lambda^d_{+,r}$ be adjacent, i.e., $N(\mathbf{u} - \mathbf{v}) = \delta$ where δ is the squared length of the minimal vectors of the lattice ($\delta = 2$ uniformly for $d = 2, 4, 8$ under the packing-radius convention $\langle \alpha, \alpha \rangle = 2$ of Section 2). Then*

$$N\big(\iota_r(\mathbf{u}) - \iota_r(\mathbf{v})\big) = \frac{r^4\,\delta}{N(\mathbf{u})\,N(\mathbf{v})}.$$

This follows by direct expansion. Writing the difference over a common denominator,

$$\iota_r(\mathbf{u}) - \iota_r(\mathbf{v}) = r^2\left(\frac{\mathbf{u}}{N(\mathbf{u})} - \frac{\mathbf{v}}{N(\mathbf{v})}\right) = \frac{r^2}{N(\mathbf{u})\,N(\mathbf{v})}\big(\mathbf{u}\,N(\mathbf{v}) - \mathbf{v}\,N(\mathbf{u})\big),$$

 doi:10.20944/preprints202605.2108.v1

so $N(\iota_r(\mathbf{u}) - \iota_r(\mathbf{v})) = r^4 \, \|\mathbf{u}\, N(\mathbf{v}) - \mathbf{v}\, N(\mathbf{u})\|^2 / (N(\mathbf{u})\, N(\mathbf{v}))^2$. *The numerator factors by polarization: writing* $\langle \mathbf{u}, \mathbf{v} \rangle$ *for the Euclidean inner product and using* $N(\mathbf{u} - \mathbf{v}) = N(\mathbf{u}) - 2\langle \mathbf{u}, \mathbf{v} \rangle + N(\mathbf{v})$,

$$\begin{aligned} \|\mathbf{u}\, N(\mathbf{v}) - \mathbf{v}\, N(\mathbf{u})\|^2 &= N(\mathbf{u})\, N(\mathbf{v})^2 - 2\langle \mathbf{u}, \mathbf{v} \rangle\, N(\mathbf{u})\, N(\mathbf{v}) + N(\mathbf{v})\, N(\mathbf{u})^2 \\ &= N(\mathbf{u})\, N(\mathbf{v}) \left(N(\mathbf{u}) - 2\langle \mathbf{u}, \mathbf{v} \rangle + N(\mathbf{v}) \right) = N(\mathbf{u})\, N(\mathbf{v})\, N(\mathbf{u} - \mathbf{v}). \end{aligned}$$

Substituting this back gives

$$N(\iota_r(\mathbf{u}) - \iota_r(\mathbf{v})) = r^4 \cdot \frac{N(\mathbf{u})\, N(\mathbf{v})\, N(\mathbf{u} - \mathbf{v})}{(N(\mathbf{u})\, N(\mathbf{v}))^2} = r^4 \cdot \frac{N(\mathbf{u} - \mathbf{v})}{N(\mathbf{u})\, N(\mathbf{v})} = \frac{r^4\, \delta}{N(\mathbf{u})\, N(\mathbf{v})}.$$

The identity quantifies how nearest-neighbor distances are transformed in the inner zone and is used in the computational verification of adjacency preservation.

The adjacency norm identity quantifies how nearest-neighbor distances transform under ι_r: an outer zone edge of squared length δ is mapped to an image of squared length $\frac{r^4 \delta}{N(\mathbf{u}) N(\mathbf{v})}$. The scaling factor is always positive and depends only on the norms of the endpoints, but in general it is *not* equal to δ. Hence the image of an outer zone nearest-neighbor edge is generally not a nearest-neighbor edge in the native metric of the rational inner zone point cloud. The radial dual graph structure is therefore defined via a *transported edge relation*: edges in the inner zone are by construction the images of outer zone nearest-neighbor edges under ι_r, not nearest-neighbor edges in the native metric. The graph isomorphisms established in this paper (Theorems 1, 2, 3) are statements about this transported radial-dual graph structure. The algebraic fact above is what makes the transported relation well-defined and reversible, and what supports the exact computational verification of the radial dual as well as the folding of large-norm cycle clocks into compact rational representations without information loss.[1]

The full radial dual lattice graph is Λ_r^d with vertex set $\Lambda_{-,r}^d \cup \Lambda_{T,r}^d \cup \Lambda_{+,r}^d$ and edge set constructed exactly as in the 2D TQF (outer edges, inverted inner edges, and boundary-crossing edges).

Standing assumptions (used throughout this paper):

1. The origin is excluded from all graphs and zone partitions, as hyperspherical inversion is undefined at the origin. (See Remark 2 below.)
2. All constructions remain strictly inside the rational extension $\mathbb{Q} \otimes L^d$, with no approximations, floating-point drift, continuous relaxations, or information loss.
3. Unless otherwise stated, the canonical admissible radius corresponding to the minimal positive norm shell is understood ($r = \sqrt{2}$ uniformly for $d = 2, 4, 8$, corresponding to the minimal squared norm $N = 2$ under the uniform packing-radius convention $\langle \alpha, \alpha \rangle = 2$).

Enveloping Clifford algebra.

All constructions in this paper take place inside the real Clifford algebra $\mathrm{Cl}(d)$ for $d \in \{2, 4, 8\}$, with $\mathbb{R}^d$ identified with the grade-1 generator subspace of $\mathrm{Cl}(d)$ and the Euclidean squared norm $N(\cdot)$ identified with the Clifford quadratic form. The exceptional lattices A_2, D_4, E_8 are realized as the grade-1 root sub-systems of $\mathrm{Cl}(2)$, $\mathrm{Cl}(4)$, $\mathrm{Cl}(8)$ respectively, and the classical Eisenstein, Hurwitz, and Cayley integer rings are recovered as the even subalgebras $\mathrm{Cl}^+(2) \cong \mathbb{C}$, $\mathrm{Cl}^+(4) \cong \mathbb{H}$, and a chosen-orientation grade-1 generator algebra of $\mathrm{Cl}(8)$ (associative, not the non-associative octonions) acting by Clifford multiplication on the grade-1 generators. The hyperspherical inversion ι_r is Clifford-equivariant: it commutes with the natural action of the Pin group $\mathrm{Pin}(d) \subset \mathrm{Cl}(d)$ on the grade-1 generators, and the Weyl groups D_6, $2\mathcal{T}$, and $W(E_8)$ all lift to subgroups of $\mathrm{Pin}(d)$ that act equivariantly on ι_r.

[1] The geometric essence of the admissible hyperspherical inversion ι_r receives a memorable artistic visualization in M. C. Escher's 1935 lithograph *Hand with Reflecting Sphere* [8]: a spherical mirror maps the surrounding room so that distant exterior points appear compressed near the center of the reflection while points near the mirror surface map outward, with radial rays and local angles preserved.

 doi:10.20944/preprints202605.2108.v1

Consequently every theorem and remark below holds uniformly across $d \in \{2, 4, 8\}$ under this single enveloping algebra.

Convention (uniform root-length normalization).

Throughout this paper we adopt the standard packing-radius / Bourbaki convention $\langle \alpha, \alpha \rangle = 2$ (Euclidean length $\sqrt{2}$) for the minimal root vectors of all three grade-1 root sub-systems $A_2 \subset \mathrm{Cl}(2)$, $D_4 \subset \mathrm{Cl}(4)$, and $E_8 \subset \mathrm{Cl}(8)$. Equivalently, the canonical admissible inversion radius is $r = \sqrt{2}$ in every dimension, the minimal squared edge length is $\delta = 2$ uniformly, and the adjacency norm identity of Remark 1 specializes to $N(\iota_r(\mathbf{u}) - \iota_r(\mathbf{v})) = 4\,\delta/(N(\mathbf{u})N(\mathbf{v})) = 8/(N(\mathbf{u})N(\mathbf{v}))$ in every exceptional dimension. The earlier asymmetric choice ($r = 1$ for $d = 2, 4$; $r = \sqrt{2}$ for $d = 8$) and the corresponding rescaling $\mathbf{x} \mapsto \mathbf{x}/\sqrt{2}$ between E_8 and CCT conventions are eliminated as a result, since the maximally dense sphere packing in each of $\mathbb{R}^2$, $\mathbb{R}^4$, $\mathbb{R}^8$ has packing radius $\sqrt{2}/2$ times the root length under this normalization, and this uniform normalization is forced at the enveloping-algebra level by the inclusion chain $A_2 \subset D_4 \subset E_8$ of root sub-systems inside $\mathrm{Cl}(8)$.

Remark 2. *The exclusion of the origin is not merely a technical necessity that arises from the singularity of spherical inversion at zero. Rather, it constitutes a structurally enabling feature: puncturing the origin removes the unique fixed point under all radial scalings and inversions, which allows the inversion map ι_r to act as a free involution (with no fixed points outside the boundary shell) on the punctured lattice. This freedom unleashes a profound cascade of discrete symmetries and combinatorial dualities—most notably the exact bijective graph isomorphism between outer and inner zones—that would be obstructed if the origin were retained as a distinguished vertex. In this context, the punctured structure is foundational to the recursive bootstrapping of radial dual lattice graphs across exceptional dimensions and to the preservation of strict combinatorial self-duality under admissible inversion.*

3. Tri-Quarter Framework in 2D: Eisenstein Radial Dual Lattice Graphs

The original radial dual lattice graph construction is based on the Eisenstein integers in 2D via the TQF [4], which we re-express here as the action of the even subalgebra $\mathrm{Cl}^+(2) \cong \mathbb{C}$ on the grade-1 root sub-system $A_2 \subset \mathrm{Cl}(2)$. It achieves an exact bijective duality—between $\Lambda^2_{+,r}$ and $\Lambda^2_{-,r}$—that is preserved under the graph structure and serves as the inductive base for the recursive bootstrapping to higher dimensions developed in this paper.

3.1. Eisenstein Lattice Graph

Let $\omega = e^{2\pi i/3} = -\frac{1}{2} + i\frac{\sqrt{3}}{2}$ be a primitive cube root of unity. The Eisenstein integers form the ring

$$\mathbb{Z}[\omega] = \{m + n\omega \mid m, n \in \mathbb{Z}\}.$$

The associated lattice $L^2 \subset \mathbb{C} \cong \mathbb{R}^2$ is given by the explicit embedding

$$\mathbf{v} = m + n\omega = \left(m - \frac{n}{2}\right) + i\frac{n\sqrt{3}}{2},$$

with squared Euclidean norm

$$N(\mathbf{v}) = m^2 - mn + n^2 \in \mathbb{N}_0.$$

This quadratic form is positive definite and integer-valued on the lattice, and generates exact regular hexagonal shells of radius $\sqrt{k}$ for admissible integers k.

Definition 2. *The* underlying lattice graph Λ^2 *is the countably infinite undirected graph with*

- *vertices:* L^2,
- *edges: pairs* $\{\mathbf{v}, \mathbf{u}\}$ *such that* $N(\mathbf{v} - \mathbf{u}) = 2$ *(nearest-neighbor minimal vectors).*

 doi:10.20944/preprints202605.2108.v1

Remark 3. *The TQF and the radial dual construction operate on the origin-punctured complex plane* $\mathbb{C} \setminus \{0\} \cong \mathbb{R}^2 \setminus \{0\}$. *Circular inversion is undefined only at the origin, and the origin vertex is therefore excluded from the zone partitioning and from the domain of the inversion map* ι_r *in order to preserve bijectivity and the discrete combinatorial structure of the radial dual lattice graph.*

Remark 4. *The graph* Λ^2 *is the countably infinite triangular (hexagonal) grid graph on the punctured plane* $\mathbb{R}^2 \setminus \{0\}$. *Every vertex has degree 6, which corresponds to the six nearest neighbors separated by* 60° *angular intervals. The full point-group symmetry of the underlying lattice is the dihedral group* D_6 *of order 12, generated by* 60° *rotations and reflections.* D_6 *preserves the triangular lattice and acts transitively on the six minimal vectors, and more generally partitions each norm shell into finitely many orbits.*

3.2. Admissible Inversion Radius in 2D

Fix an admissible radius $r > 0$ as per Definition 1. The canonical choice is $r = \sqrt{2}$ (corresponding to $N = 2$ under the uniform root-length convention $\langle \alpha, \alpha \rangle = 2$, so the six minimal Eisenstein vectors satisfy $m^2 - mn + n^2 = 1$ and have squared Euclidean norm 2 after the rescaling $\mathbf{v} \mapsto \sqrt{2}\,\mathbf{v}$), which produces the boundary zone $\Lambda^2_{T,r} = L^2 \cap S^1_r$ containing exactly six vertices that form a regular hexagon centered at the origin.

The admissibility condition of Definition 1 guarantees that the boundary zone $\Lambda^d_{T,r} = L^d \cap S^{d-1}_r$ is a discrete, finite, and symmetry-invariant subset of L^d. This property ensures that the subsequent inversion map sends all vertices to well-defined vertices in the rational extension while preserving the discrete combinatorial structure required for the radial dual graph construction.

3.3. Zone Partitioning and Circular Inversion in 2D

Fix an admissible radius $r > 0$. The inner zone will consist of the images of the outer zone vertices under the circular inversion map $\iota_r : \mathbb{C} \setminus \{0\} \to \mathbb{C} \setminus \{0\}$ that we define explicitly in the next subsection. Then we partition the vertex set of $\Lambda^2 \setminus \{0\}$ into three disjoint subsets:

- **Outer zone**: $\Lambda^2_{+,r} = \{\mathbf{v} \in L^2 \mid N(\mathbf{v}) > r^2\}$,
- **Boundary zone**: $\Lambda^2_{T,r} = \{\mathbf{v} \in L^2 \mid N(\mathbf{v}) = r^2\} = L^2 \cap S^1_r$,
- **Inner zone**: $\Lambda^2_{-,r} = \iota_r(\Lambda^2_{+,r})$, the set of all vertices in $\mathbb{Q}(\omega)$ obtained by inversion (generally with rational coefficients in the Eisenstein basis).

The full radial dual lattice graph Λ^2_r is the undirected graph with

- vertex set is the disjoint union $V(\Lambda^2_r) = \Lambda^2_{-,r} \cup \Lambda^2_{T,r} \cup \Lambda^2_{+,r}$,
- edge set consists of (i) the outer zone nearest-neighbor edges of Λ^2, (ii) their images under ι_r in the inner zone, and (iii) crossing edges connecting boundary vertices to inverted outer vertices (defined precisely in the next subsection).

The vertices of $\Lambda^2_{-,r}$ reside in $\mathbb{Q}(\omega)$, and therefore generally carry rational (rather than integer) coefficients in the Eisenstein basis.

This partitioning creates a tripartite (or "Tri-Quarter") division of the punctured plane $\mathbb{C} \setminus \{0\}$: the outer zone $\Lambda^2_{+,r}$ consists of all lattice vertices with $N(\mathbf{v}) > r^2$ (beyond the boundary shell), the boundary zone $\Lambda^2_{T,r} = L^2 \cap S^1_r$ comprises the fixed admissible shell $N(\mathbf{v}) = r^2$, and the inner zone $\Lambda^2_{-,r}$ is the exact algebraic image of $\Lambda^2_{+,r}$ under inversion of ι_r through the circle S^1_r of radius r.

The inversion map ι_r is given in Section 2 and satisfies the five algebraic properties listed there. In the context of the Eisenstein lattice L^2 and the TQF [4,9], the map is conformal and angle-preserving, thereby respecting the 60° angular structure inherent to the triangular lattice L^2.

Geometrically, ι_r radially rescales every vertex $\mathbf{v} \in \Lambda^2_r$ through the circle S^1_r of radius r: any vertex $\mathbf{v} \in \Lambda^2_{+,r}$ that exists far outside the boundary $\Lambda^2_{T,r}$ is mapped to $\mathbf{v}' = \iota_r(\mathbf{v}) \in \Lambda^2_{-,r}$, which is close to the origin along the same radial ray, and vice versa. Because the map acts as a positive scalar multiple of the identity on each ray, it preserves radial directions and the discrete structure required for the radial dual lattice graph construction [4].

 doi:10.20944/preprints202605.2108.v1

3.4. Construction and Duality in 2D

The edge set $E(\Lambda^2_r)$ of the radial dual lattice graph is defined in three parts:

- **Outer zone edges**: all nearest-neighbor edges of Λ^2 with both endpoints in $\Lambda^2_{+,r}$,
- **Inner zone edges**: the images $\{\iota_r(\mathbf{v}), \iota_r(\mathbf{u})\}$ of every outer zone edge $\{\mathbf{v}, \mathbf{u}\}$,
- **Boundary crossing edges**: for each pair consisting of a boundary vertex $\mathbf{v} \in \Lambda^2_{T,r}$ and an outer vertex $\mathbf{u} \in \Lambda^2_{+,r}$ that are adjacent in Λ^2, add the edge $\{\mathbf{v}, \iota_r(\mathbf{u})\}$.

Theorem 1 (2D Bijective Radial Graph Duality [4]). *For any admissible r, the restriction of ι_r induces an isomorphism between the induced subgraphs of the transported radial-dual graph structure on the outer and inner zones:*

$$\iota_r \colon (\Lambda^2_{+,r}, E(\Lambda^2_r)|_{\Lambda^2_{+,r}}) \;\to\; (\Lambda^2_{-,r}, E(\Lambda^2_r)|_{\Lambda^2_{-,r}}).$$

Proof. The map ι_r is an algebraic involution that swaps $\Lambda^2_{+,r}$ and $\Lambda^2_{-,r}$ bijectively. By construction of the edge set, every outer zone nearest-neighbor edge maps directly to an inner zone edge under the transported edge relation defined in Section 2. Boundary-crossing edges are mirrored symmetrically via the involution property and fixed boundary.

The dihedral symmetry group D_6 commutes with ι_r because circular inversion through an origin-centered admissible shell is conformal and angle-preserving, and the lattice is D_6-invariant. Therefore ι_r is a graph isomorphism between the induced subgraphs in the transported radial-dual graph structure (see also Remark 4); native-metric nearest-neighbor adjacency of the inner zone point cloud is generally not preserved. □

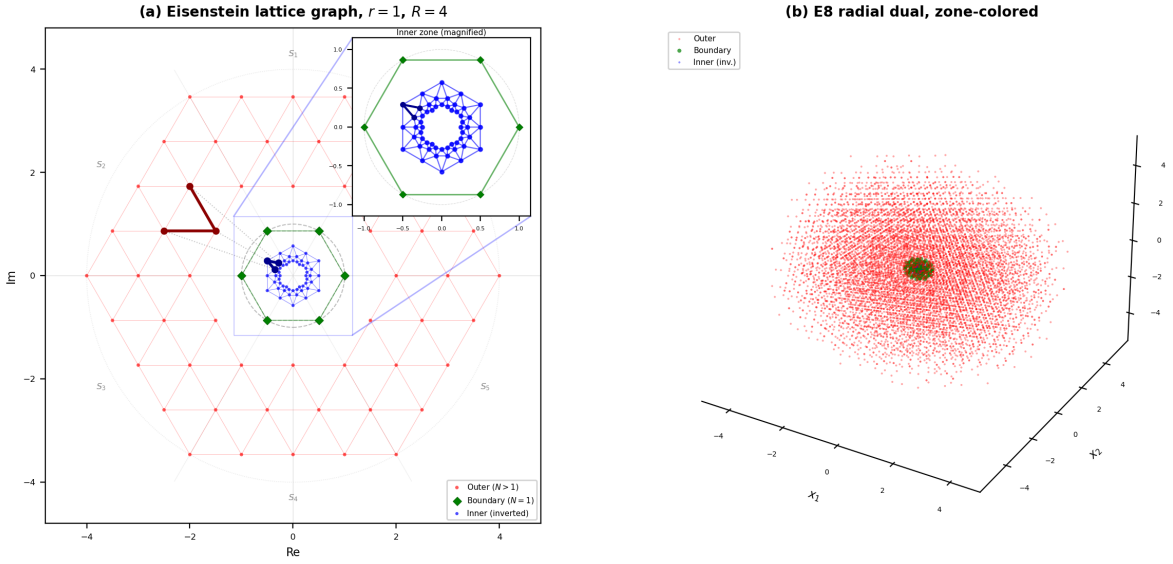

Figure 1. Radial dual lattice graphs with zone-colored edges. **(a)** Eisenstein lattice graph with $r = 1$, $R = 4$. Red/blue edges show the graph isomorphism between $\Lambda^2_{+,r}$ and $\Lambda^2_{-,r}$ (boundary shell $\Lambda^2_{T,r} = L^2 \cap S^1_r$). Inset: magnified $\Lambda^2_{-,r}$. **(b)** E_8 radial dual projected to 3D via $H_{4\text{fold}}$, inversion, and FIG slice, zone-colored to match.

Having established the foundational 2D case via the TQF and verified its exact bijective radial duality in Theorem 1, we now extend the construction recursively to the next exceptional dimension by bootstrapping from the Eisenstein integers to the Hurwitz quaternions.

4. Bootstrapping to 4D: Radial Dual Hurwitz Quaternion Lattice Graphs

The construction and proof that were established for the Eisenstein integers in 2D extend verbatim to the Hurwitz quaternion lattice in 4D. The admissible hyperspherical inversion ι_r induces an exact transported-edge graph isomorphism between the outer zone and inner zone induced subgraphs,

 doi:10.20944/preprints202605.2108.v1

preserving transported adjacency, norms of pre-images, radial directions, and the binary tetrahedral symmetry group $2\mathcal{T}$.

4.1. Hurwitz Quaternion Lattice Graph

The even subalgebra $\mathrm{Cl}^+(4) \cong \mathbb{H}$ furnishes a natural algebraic environment for rotations in 3D space; equivalently, quaternions extend the complex numbers from 2D to 4D as the even Clifford subalgebra over the D_4 grade-1 generators. The Hurwitz integers form the densest lattice packing in 4D. They comprise all quaternions

$$\mathbf{q} = a + bi + cj + dk, \quad a, b, c, d \in \tfrac{1}{2}\mathbb{Z},$$

such that $a + b + c + d \in \mathbb{Z}$. The associated lattice $L^4 \subset \mathbb{R}^4$ carries the norm $N(\mathbf{q}) = a^2 + b^2 + c^2 + d^2$.

Definition 3. *The* underlying lattice graph Λ^4 *is the countably infinite undirected graph with*

- *vertices:* L^4,
- *edges: pairs* $\{\mathbf{q}, \mathbf{p}\}$ *such that* $N(\mathbf{q} - \mathbf{p}) = 2$ *(nearest-neighbor minimal vectors).*

Each vertex has degree 24. Under the uniform root-length convention $\langle \alpha, \alpha \rangle = 2$, these 24 nearest-neighbor minimal vectors are the $N = 2$ shell vectors—the permutations of $(\pm 1, \pm 1, 0, 0)$, which constitute the D_4 root system and the vertex set of the regular 24-cell—and should be distinguished from the 24 multiplicative units of $\mathbb{H}$, which form the $N = 1$ shell (the 8 vectors $\pm \mathbf{e}_i$ together with the 16 half-integer vectors $(\pm\frac{1}{2}, \pm\frac{1}{2}, \pm\frac{1}{2}, \pm\frac{1}{2})$). The minimal edge length $\delta = 2$ adopted here is consistent with the 2D and 8D constructions and with the uniform convention of Section 2.

4.2. Admissible Inversion Radius in 4D

Fix an admissible radius $r > 0$ as per Definition 1. The canonical choice $r = \sqrt{2}$ yields the boundary zone $\Lambda^4_{T,r} = L^4 \cap S^3_r$ containing the 24 vertices of squared norm 2 (under the uniform root-length convention $\langle \alpha, \alpha \rangle = 2$), which form the vertex set of the regular 24-cell after the global rescaling $\mathbf{q} \mapsto \sqrt{2}\,\mathbf{q}$.

Admissibility guarantees that the boundary zone $\Lambda^4_{T,r} = L^4 \cap S^3_r$ is a discrete, finite, and symmetry-invariant subset of L^4.

4.3. Zone Partitioning and Hyperspherical Inversion in 4D

The same tripartite division applied in 2D extends directly to 4D. Thus, we prepare for an inductive transfer of the bijective duality established in Theorem 1.

Fix an admissible radius $r > 0$. The inner zone will consist of the images of the outer zone vertices under the hyperspherical inversion map $\iota_r : \mathbb{H} \setminus \{0\} \to \mathbb{H} \setminus \{0\}$ that we define explicitly in the next subsection. Partition the vertex set of $\Lambda^4 \setminus \{0\}$ into three disjoint subsets exactly as in the 2D case:

- **Outer zone**: $\Lambda^4_{+,r} = \{\mathbf{q} \in L^4 \mid N(\mathbf{q}) > r^2\}$,
- **Boundary zone**: $\Lambda^4_{T,r} = \{\mathbf{q} \in L^4 \mid N(\mathbf{q}) = r^2\} = L^4 \cap S^3_r$,
- **Inner zone**: $\Lambda^4_{-,r} = \iota_r(\Lambda^4_{+,r})$, the set of all vertices in the rational extension $\mathbb{Q} \otimes_{\mathbb{Z}} \mathbb{H}$ obtained by inversion.

The full radial dual lattice graph Λ^4_r is the undirected graph with

- vertex set is the disjoint union $V(\Lambda^4_r) = \Lambda^4_{-,r} \cup \Lambda^4_{T,r} \cup \Lambda^4_{+,r}$,
- edge set consists of (i) the outer zone nearest-neighbor edges of Λ^4, (ii) their images under ι_r in the inner zone, and (iii) crossing edges connecting boundary vertices to inverted outer vertices (defined precisely in the next subsection).

The vertices of $\Lambda^4_{-,r}$ reside in the rational extension $\mathbb{Q} \otimes_{\mathbb{Z}} \mathbb{H}$, and therefore generally carry rational (rather than half-integer) coefficients in the Hurwitz basis.

 doi:10.20944/preprints202605.2108.v1

The inversion map ι_r is given in Section 2 and satisfies the five algebraic properties listed there. This is the direct 4D analogue of the circular inversion in 2D: each vertex is reflected through S_r^3 with radius r centered at the origin. Consequently, vertices that exist far outside the boundary shell are mapped close to the origin along the identical radial ray, and vice versa.

The map remains conformal and commutes with the natural action of $\mathrm{SU}(2) \times \mathrm{SU}(2)$ on $\mathbb{H}$, thereby preserving the angular and combinatorial structure required for the radial dual lattice graph construction.

4.4. Construction and Duality in 4D

The edge set $E(\Lambda_r^4)$ of the radial dual lattice graph is defined exactly as in the 2D case:

- **Outer zone edges**: all nearest-neighbor edges of Λ^4 with both endpoints in $\Lambda^4_{+,r}$,
- **Inner zone edges**: the images $\{\iota_r(\mathbf{q}), \iota_r(\mathbf{p})\}$ of every outer zone edge $\{\mathbf{q}, \mathbf{p}\}$,
- **Boundary crossing edges**: for each pair consisting of a boundary vertex $\mathbf{p} \in \Lambda^4_{T,r}$ and an outer vertex $\mathbf{q} \in \Lambda^4_{+,r}$ that are adjacent in Λ^4, add the edge $\{\mathbf{p}, \iota_r(\mathbf{q})\}$.

Remark 5 (Adjacency norm identity in 4D)**.** *With canonical radius $r = \sqrt{2}$ ($\Rightarrow r^4 = 4$) and minimal squared length $\delta = 2$, Remark 1 specializes to*

$$N\big(\iota_r(\mathbf{q}) - \iota_r(\mathbf{p})\big) = \frac{8}{N(\mathbf{q})\,N(\mathbf{p})}$$

for any adjacent vertices $\mathbf{p}, \mathbf{q} \in \Lambda^4_{+,r}$.

Theorem 2 (4D Bijective Radial Graph Duality)**.** *For any admissible r, the restriction of ι_r induces an isomorphism between the induced subgraphs of the transported radial-dual graph structure on the outer and inner zones:*

$$\iota_r \colon (\Lambda^4_{+,r}, E(\Lambda_r^4)|_{\Lambda^4_{+,r}}) \to (\Lambda^4_{-,r}, E(\Lambda_r^4)|_{\Lambda^4_{-,r}}).$$

Proof. The map ι_r is an algebraic involution that swaps $\Lambda^4_{+,r}$ and $\Lambda^4_{-,r}$ bijectively. By construction of the edge set, every outer zone nearest-neighbor edge maps directly to an inner zone edge under the transported edge relation. Boundary-crossing edges are mirrored symmetrically via the involution property and fixed boundary.

The order-24 binary tetrahedral group $2\mathcal{T}$ commutes with ι_r because hyperspherical inversion through an origin-centered admissible shell is equivariant under the natural action of $\mathrm{SU}(2) \times \mathrm{SU}(2)$ on $\mathbb{H}$. Therefore ι_r is a graph isomorphism between the induced subgraphs in the transported radial-dual graph structure; native-metric nearest-neighbor adjacency of the inner zone point cloud is generally not preserved. □

The natural symmetry group that acts on the Hurwitz quaternion lattice L^4 (and therefore on the radial dual lattice graph Λ_r^4) is the order-24 binary tetrahedral group $2\mathcal{T}$. This group commutes with ι_r because the admissible inversion radius is origin-centered and the map ι_r is equivariant under left–right unit multiplications on $\mathbb{H}$.

Remark 6 (Orthogonal splicing (2D to 4D))**.** *An alternative view of the same duality may be obtained by orthogonally embedding each 2D dual pair $(\mathbf{v}_+, \iota_r(\mathbf{v}_+))$, where $\mathbf{v}_+ \in \Lambda^2_{+,r}$, as the quaternion*

$$\mathbf{q} = \mathbf{v}_+ + \iota_r(\mathbf{v}_+)j \in \mathbb{Q} \otimes_{\mathbb{Z}} \mathbb{H}.$$

The resulting graph is isomorphic to a (non-canonical) subgraph of the full 4D radial dual Λ_r^4 and illustrates the recursive lifting of the 2D structure, but the canonical construction used throughout this paper operates directly on the Hurwitz lattice L^4.

 doi:10.20944/preprints202605.2108.v1

Now that we've verified that the radial dual lattice graph construction and the induced bijective graph isomorphism extend verbatim from the Eisenstein integers in 2D to the Hurwitz quaternions in 4D, we now proceed to the final exceptional dimension.

5. Bootstrapping to 8D: Radial Dual E_8 Lattice Graphs

The construction and proof established for the Eisenstein integers in 2D and the Hurwitz quaternions in 4D extend verbatim to the E_8 root lattice in 8D. The admissible hyperspherical inversion ι_r induces an exact transported-edge graph isomorphism between the outer zone and inner zone induced subgraphs, preserving transported adjacency, norms of pre-images, radial directions, and the full Weyl group symmetry $W(E_8)$.

5.1. E_8 Lattice Graph

The E_8 root lattice $L^8 \subset \mathbb{R}^8$ is the unique (up to isomorphism) even unimodular lattice in 8D. In the standard coordinate realization it consists of all vectors $\mathbf{x} = (\mathbf{x}_1, \ldots, \mathbf{x}_8) \in \mathbb{Z}^8 \cup (\mathbb{Z} + \frac{1}{2})^8$ whose coordinate sum is even. Equivalently, it arises from pairs of Hurwitz quaternions $(\mathbf{p}, \mathbf{q}) \in \mathbb{H}^2$ satisfying the gluing condition $\mathbf{p} + \mathbf{q} \in (1+i)\mathbb{H}$. The lattice is even (all squared norms are even integers) and self-dual ($L^8 = (L^8)^*$). It realizes the densest known sphere packing in $\mathbb{R}^8$.

Its 240 vectors of squared Euclidean norm 2—the roots—split into 112 vectors of $\mathcal{D}_8$ "checkerboard" sub-lattice type ($\pm\mathbf{e}_i \pm \mathbf{e}_j$, $i < j$) and 128 half-integer vectors ($\pm\frac{1}{2}, \ldots, \pm\frac{1}{2}$) with an even number of minus signs. These minimal vectors generate the E_8 root system and achieve the kissing number 240.

Definition 4. *The* underlying lattice graph Λ^8 *is the countably infinite undirected graph with*

- *vertices:* L^8,
- *edges: pairs* $\{\mathbf{x}, \mathbf{y}\}$ *such that* $N(\mathbf{x} - \mathbf{y}) = 2$ *(nearest-neighbor minimal vectors).*

Each vertex has degree 240. The full isometry group of L^8 is the Weyl group $W(E_8)$ of order 696 729 600, which acts transitively on the roots and preserves the graph structure.

5.2. Octonionic Realization via Cayley Integers

The E_8 root lattice L^8 admits a canonical realization as the grade-1 root sub-system of the real Clifford algebra $\mathrm{Cl}(8)$; equivalently, by choosing an orientation of the generators, it can be identified with the lattice of *Cayley integers* (integral octonions [10]) inside the real division algebra $\mathbb{O}$, but the Clifford-algebraic realization is preferred throughout because it is associative and supplies the natural enveloping algebra under which A_2, D_4, and E_8 share a single uniform root-length normalization. We adopt throughout this paper the standard E_8 normalization in which the minimal vectors (roots) satisfy $N(\mathbf{x}) = 2$ and therefore have Euclidean length $\sqrt{2}$. With this convention, the lattice L^8 contains all Cayley integers with even norm, and the admissible boundary zone $\Lambda^8_{T,r} = L^8 \cap S^7_r$ (with $r = \sqrt{2}$) consists precisely of the 240 minimal vectors (roots of squared norm 2). We note that the term "unit" is ambiguous in this context: in the octonion-algebra sense, a unit is a multiplicative norm-one element, of which there are 240 in the Cayley integers after rescaling by $1/\sqrt{2}$; in this paper, the 240 minimal vectors are roots of squared norm 2 under the E_8 normalization. Under the Clifford-algebraic $\mathrm{Cl}(8)$ formulation adopted in this paper, all three exceptional-lattice constructions arise as the grade-1 root sub-systems of $\mathrm{Cl}(2)$, $\mathrm{Cl}(4)$, and $\mathrm{Cl}(8)$ respectively, and share the same packing-radius root-length normalization $\langle \alpha, \alpha \rangle = 2$ (Euclidean length $\sqrt{2}$); no rescaling between dimensions is required, and all radial-dual identities (involution, zone swap, transported-edge isomorphism) hold uniformly under the action of $\mathrm{Pin}(d) \subset \mathrm{Cl}(d)$.

Now the radial dual lattice graph construction never invokes octonion multiplication. Instead, it relies solely on the Euclidean quadratic form $N(\cdot)$ and ordinary radial scaling $\mathbf{x} \mapsto \lambda\mathbf{x}$ ($\lambda \in \mathbb{Q}_{>0}$), both of which remain well-defined and associative over $\mathbb{R}$. Consequently, every operation stays inside the rational extension $\mathbb{Q} \otimes_{\mathbb{Z}} L^8$ and admits exact finite-precision arithmetic. All algebraic properties established in lower dimensions (involution, zone swapping, norm relation, angular preservation,

 doi:10.20944/preprints202605.2108.v1

and symmetry commutation) hold verbatim on this structure. The vertices of $\Lambda^8_{-,r}$ lie in the rational octonions $\mathbb{Q} \otimes_{\mathbb{Z}} \mathbb{O}$, where they uphold discreteness, countability, and the transported-edge graph isomorphism of Theorem 3.

Remark 7 (Octonionic coordinate embedding of E_8 with native CCT integration)**.** *The standard construction of the E_8 root lattice as the set of Cayley integers (i.e., integral octonions) solidifies a natural conceptual link to the octonion-based models employed in CCT and related emergence programs [11,12]. This link is achieved while fully persisting the exact discrete, rational, and reversible character that constitutes the central strength of the present framework. In particular, the construction seamlessly integrates with CCT's deliberate choice of the associative Clifford algebra* $\mathrm{Cl}(8)$ *as its primary operational algebra. Consequently, the Cayley integers serve as a distinct trustworthy coordinate vertex set that encodes both the exceptional geometry of the E_8 root lattice L^8 and its maximal symmetry group $W(E_8)$.*

5.3. Admissible Inversion Radius in 8D

Fix an admissible radius $r > 0$ as per Definition 1. The canonical and optimal choice is $r = \sqrt{2}$ (corresponding to $N = 2$, the root shell), which exactly coincides with the boundary zone $\Lambda^8_{T,r} = L^8 \cap S^7_r$ containing the 240 roots.

The admissibility condition of Definition 1 guarantees that the boundary zone $\Lambda^8_{T,r} = L^8 \cap S^7_r$ is a discrete, finite, and symmetry-invariant subset of L^8. This property ensures that the subsequent inversion map sends all vertices to well-defined vertices in the rational extension while maintaining the discrete combinatorial structure that is required to construct the radial dual graph.

This shell is invariant under the full Weyl group $W(E_8)$. Every nonzero norm shell of L^8 is also $W(E_8)$-invariant (since $W(E_8)$ preserves the norm), so higher admissible shells (e.g., $N = 4$) do not reduce the available symmetry. What does grow at higher shells is the orbit complexity, shell multiplicity, denominator complexity of inner zone images, and overall computational cost. The canonical choice $r = \sqrt{2}$ is therefore optimal in a computational sense—it produces the smallest nontrivial boundary set with $W(E_8)$ invariance—rather than in a symmetry sense. In this first-principles approach, we wish to maximize computational tractability while retaining the full symmetry group.

5.4. Zone Partitioning and Hyperspherical Inversion in 8D

Fix an admissible radius $r > 0$. Just as in the 2D and 4D environments, the origin remains excluded (Remark 3). Hence, inversion map ι_r is rendered well-defined on all nonzero lattice points.

The inner zone consists of the images of the outer zone vertices under the hyperspherical inversion map $\iota_r : \mathbb{R}^8 \setminus \{0\} \to \mathbb{R}^8 \setminus \{0\}$. We partition the vertex set of $\Lambda^8 \setminus \{0\}$ into three disjoint subsets:

- **Outer zone**: $\Lambda^8_{+,r} = \{\mathbf{x} \in L^8 \mid N(\mathbf{x}) > r^2\}$,
- **Boundary zone**: $\Lambda^8_{T,r} = \{\mathbf{x} \in L^8 \mid N(\mathbf{x}) = r^2\} = L^8 \cap S^7_r$,
- **Inner zone**: $\Lambda^8_{-,r} = \iota_r(\Lambda^8_{+,r}) \subset \mathbb{Q} \otimes L^8$,

where admissibility of r ensures that every vertex in $\Lambda^8_{+,r}$ is sent to a well-defined vertex in the rational extension $\mathbb{Q} \otimes L^8$, and the image set remains discrete and countable.

The full radial dual lattice graph Λ^8_r is the undirected graph with

- vertex set is the disjoint union $V(\Lambda^8_r) = \Lambda^8_{-,r} \cup \Lambda^8_{T,r} \cup \Lambda^8_{+,r}$,
- edge set consists of (i) the outer zone nearest-neighbor edges of Λ^8, (ii) their images under ι_r in the inner zone, and (iii) crossing edges connecting boundary vertices to inverted outer vertices (defined precisely in the next subsection).

The vertices of $\Lambda^8_{-,r}$ reside in the rational extension $\mathbb{Q} \otimes L^8$, and therefore generally carry rational coefficients in the E_8 coordinate basis.

The inversion map ι_r is given in Section 2 and satisfies the five algebraic properties listed there. This is the direct higher-dimensional analogue of circular inversion in 2D and hyperspherical inversion in 4D: each vertex is reflected through the origin-centered hypersphere S^7_r of radius r, which sends

 doi:10.20944/preprints202605.2108.v1

distant vertices close to the origin (and vice versa) while preserving the ray from the origin on which the vertex lives.

No octonionic conjugation is involved because the transformation is simply a positive rational scaling of the vector $\mathbf{x}$ itself. All operations therefore remain well-defined and associative over the reals, and the vertices of the inner zone $\Lambda^8_{-,r}$ lie in the rational extension $\mathbb{Q} \otimes L^8$ while preserving discreteness and countability.

These properties are directly exploited in the inductive proof of the 8D graph isomorphism (Theorem 3) and the adjacency norm identity (Remark 5).

5.5. Construction and Duality in 8D

The edge set $E(\Lambda^8_r)$ of the radial dual lattice graph is defined exactly as in the 2D and 4D cases:

- **Outer zone edges**: all nearest-neighbor edges of Λ^8 with both endpoints in $\Lambda^8_{+,r}$,
- **Inner zone edges**: the images $\{\iota_r(\mathbf{x}), \iota_r(\mathbf{y})\}$ of every outer zone edge $\{\mathbf{x}, \mathbf{y}\}$,
- **Boundary crossing edges**: for each pair consisting of a boundary vertex $\mathbf{y} \in \Lambda^8_{T,r}$ and an outer vertex $\mathbf{x} \in \Lambda^8_{+,r}$ that are adjacent in Λ^8, add the edge $\{\mathbf{y}, \iota_r(\mathbf{x})\}$.

Theorem 3 (8D Bijective Radial Graph Duality)**.** *For any admissible r, the restriction of ι_r induces an isomorphism between the induced subgraphs of the transported radial-dual graph structure on the outer and inner zones:*

$$\iota_r \colon (\Lambda^8_{+,r}, E(\Lambda^8_r)|_{\Lambda^8_{+,r}}) \to (\Lambda^8_{-,r}, E(\Lambda^8_r)|_{\Lambda^8_{-,r}}).$$

Proof. The map ι_r is an algebraic involution that swaps $\Lambda^8_{+,r}$ and $\Lambda^8_{-,r}$ bijectively. By construction of the edge set, every outer zone nearest-neighbor edge maps directly to an inner zone edge under the transported edge relation. Boundary-crossing edges are mirrored symmetrically via the involution property and fixed boundary. The Weyl group $W(E_8)$ commutes with ι_r because (i) the admissible shell is origin-centered, (ii) L^8 is self-dual, and (iii) central inversion $\mathbf{x} \mapsto -\mathbf{x}$ (already in $W(E_8)$) is compatible with radial scaling along every ray. Consequently, the restriction of ι_r is equivariant under $W(E_8)$, ensuring that it induces a graph isomorphism in the transported radial-dual graph structure that preserves transported adjacency, radial directions, norms of pre-images, and the transported combinatorial invariants of the lattice graph; native-metric nearest-neighbor adjacency of the inner zone point cloud is generally not preserved. □

The full isometry group of the E_8 root lattice L^8 (and therefore of the radial dual lattice graph Λ^8_r) is the Weyl group $W(E_8)$ of order 696 729 600. This group commutes with ι_r for the canonical admissible radius $r = \sqrt{2}$ because the inversion is equivariant under all lattice isometries that fix the origin.

Remark 8 (Orthogonal splicing (4D to 8D))**.** *An alternative view of the same duality may be obtained by orthogonally embedding each 4D dual pair $(\mathbf{q}_+, \iota_r(\mathbf{q}_+))$, where $\mathbf{q}_+ \in \Lambda^4_{+,r}$, as the Cayley integer*

$$\mathbf{x} = \mathbf{q}_+ + \iota_r(\mathbf{q}_+)\ell \in \mathbb{Q} \otimes_{\mathbb{Z}} \mathbb{O},$$

where ℓ is a suitable imaginary octonion unit orthogonal to the quaternion subalgebra. The resulting graph is isomorphic to a (non-canonical) subgraph of the full 8D radial dual Λ^8_r and illustrates the recursive lifting of the 4D structure, but the canonical construction used throughout this paper operates directly on the E_8 root lattice L^8.

Remark 9 (Adjacency norm identity in 8D)**.** *With canonical radius $r = \sqrt{2}$ ($\Rightarrow r^4 = 4$) and minimal squared length $\delta = 2$, Remark 1 specializes to*

$$N\big(\iota_r(\mathbf{x}) - \iota_r(\mathbf{y})\big) = \frac{8}{N(\mathbf{x})\,N(\mathbf{y})}$$

 doi:10.20944/preprints202605.2108.v1

for any adjacent vertices $\mathbf{x}, \mathbf{y} \in \Lambda^8_{+,r}$.

The properties established above—in particular the involution property, zone-swapping bijection, angular preservation, norm inversion relation $N(\iota_r(\mathbf{x})) = r^4/N(\mathbf{x})$, and induced transported-edge graph isomorphism between the outer and inner zone subgraphs (Theorem 3)—together define a reversible coordinate-compression operator. This operator maps any finite outer zone subgraph (regardless of radial extent) to an inner zone subgraph whose vertex coordinates are rational with denominators controlled by the norms of the original vertices. The resulting structure is therefore particularly well-suited to exact graph algorithms that must operate at arbitrarily large radii while remaining memory-efficient under exact rational arithmetic.

6. Linear Folding of E_8 via the Moxness H_4 Folding Matrix

High-dimensional vertex sets of lattices and their nearest-neighbor graphs arise frequently in discrete geometry, data modeling, and exact simulation frameworks. To streamline implementation, reduce computational complexity, and improve efficiency, a common strategy is to reduce dimensionality while preserving the exact adjacency relations, symmetry groups, and selected metric properties.

A particularly effective linear folding operator for the E_8 root lattice $L^8 \subset \mathbb{R}^8$ and its associated nearest-neighbor graph Λ^8 is realized by the invertible 8×8 real matrix $H_{4\text{fold}}$ introduced by Moxness [7]. Its top 4×8 block Π, the *projection block*, sends each lattice vertex $\mathbf{x} \in \mathbb{Q} \otimes L^8$ to a 4D vertex $\mathbf{q} = \Pi\mathbf{x}$ over the quadratic field $\mathbb{Q}(\sqrt{5})$; on the 240 roots of L^8, Π is computationally verified to be bijective onto the union of the vertices of the regular 600-cell H_4 and its golden-ratio scaled copy $H_4\Phi$ (radius ratio Φ; equivalently, squared-norm ratio Φ^2). This projection lands naturally in the rational extension $\mathbb{Q} \otimes_{\mathbb{Z}} \mathbb{H}$ already employed for the 4D radial dual lattice graph Λ^4_r (Section 4), thereby allowing the inherited 4D hyperspherical inversion ι_r to be applied directly in the quaternion setting.

On the root shell, this folding collapses the 8D root system into two interpenetrating self-similar 4D polytopes that uphold the same combinatorial structure, kissing number, nearest-neighbor distances (up to global scaling), and symmetry invariants in half the dimensional encoding. The full 8×8 matrix $H_{4\text{fold}}$ is invertible as a linear transformation of $\mathbb{R}^8$; the top 4×8 block Π alone is a rank-4 projection with a 4-dimensional kernel and is therefore not invertible as a map $\mathbb{R}^8 \to \mathbb{R}^4$. Exact reversibility on the root shell, where Π is verified bijective onto $H_4 \cup H_4\Phi$, is a finite-shell computational statement rather than a global linear-algebra inverse. Critically, the linear map Π composes algebraically with the nonlinear radial inversion ι_r (Section 2) to produce a composite folding operator that simultaneously delivers dimensional reduction and radial coordinate compression on tested finite domains. This combination is especially valuable in CCT because it enables compact representations of moderate-norm cycle clocks while feeding directly into existing 4D-to-3D projection pipelines (e.g., Fibonacci icosagrid slices).

6.1. The Moxness Folding Matrix and Projection Block

Let $\Phi = (1+\sqrt{5})/2$ and $\phi = \Phi - 1 = (\sqrt{5}-1)/2$. The symmetric folding matrix is defined as

$$H_{4\text{fold}} = \begin{pmatrix} \Phi & 0 & 0 & 0 & \phi^2 & 0 & 0 & 0 \\ 0 & \phi & 1 & 0 & 0 & -\phi & 1 & 0 \\ 0 & 1 & 0 & \phi & 0 & 1 & 0 & -\phi \\ 0 & 0 & \phi & 1 & 0 & 0 & -\phi & 1 \\ \phi^2 & 0 & 0 & 0 & \Phi & 0 & 0 & 0 \\ 0 & -\phi & 1 & 0 & 0 & \phi & 1 & 0 \\ 0 & 1 & 0 & -\phi & 0 & 1 & 0 & \phi \\ 0 & 0 & -\phi & 1 & 0 & 0 & \phi & 1 \end{pmatrix}. \tag{1}$$

 doi:10.20944/preprints202605.2108.v1

Let $\Pi \in \mathbb{R}^{4\times 8}$ denote the top four rows of $H_{4\text{fold}}$ (the projection block). For any vertex $\mathbf{x} \in \mathbb{Q} \otimes L^8$, the linearly folded image is

$$\mathbf{q} = \Pi\mathbf{x} \in \mathbb{Q}(\sqrt{5})^4. \tag{2}$$

The matrix $H_{4\text{fold}}$ satisfies $H_{4\text{fold}} = H_{4\text{fold}}^{\dagger}$ and is invertible as an 8×8 linear transformation, so given the *full* 8-vector $H_{4\text{fold}}\mathbf{x}$ (both 4D components), the original 8D coordinates can be recovered exactly. The top-block projection Π alone retains only four of these eight components and has a nontrivial 4-dimensional kernel in $\mathbb{R}^8$; recovery of $\mathbf{x}$ from $\mathbf{q} = \Pi\mathbf{x}$ alone is therefore not possible in general.

Proposition 1 (Bijective mapping of the root shell; finite-shell verified)**.** *The restriction of Π to the 240 roots of L^8 (boundary zone $\Lambda^8_{T,r}$ with canonical admissible radius $r = \sqrt{2}$) is a bijection onto the vertex set of $H_4 \cup H_4\Phi$. The squared Euclidean norms $\|\Pi\mathbf{x}\|^2$ of the projected vectors take exactly two distinct values, $6 - 2\sqrt{5}$ and 4, each attained 120 times; their ratio is Φ^2, and consequently the radii of the two 600-cell layers stand in the ratio Φ.*

Verification. Direct computation in exact $\mathbb{Q}(\sqrt{5})$ arithmetic on all 240 roots; see Section 8.1 (Part 2) and the supplementary script `verify_h4_norm_ratio.py`. □

This exact bijection is confirmed computationally in Section 8.1 (Part 2) using exact rational arithmetic. Geometrically, the 600-cell realizes the densest known sphere packing in 4D, and the golden-ratio scaling $H_4\Phi$ naturally encodes the pentagonal/quasicrystalline symmetry already present in E_8. Thus, on the root shell, the linear folding operator provides an algebraically clean coordinate transformation that halves per-vertex storage and arithmetic cost while preserving all invariants required for CCT modeling of the 240-root configuration.

Remark 10 (Arithmetic origin of the golden folding: the icosian construction of E_8)**.** *The appearance of the golden ratio Φ in the folding block Π is not a coordinate artifact but reflects a third standard construction of E_8. Beyond the D_8-coset and Cayley-integer descriptions used elsewhere in this paper, E_8 is isomorphic, as a rank-8 $\mathbb{Z}$-lattice, to the icosian ring $\mathcal{I}$: a rank-4 free module over $\mathbb{Z}[\tau]$ ($\tau = \Phi$) equipped with a $\mathbb{Z}$-valued trace form, whose underlying lattice is exactly E_8 [16]. Under this identification the golden-ratio rescaling $H_4 \mapsto H_4\Phi$ is multiplication by the fundamental unit τ of $\mathbb{Z}[\tau]$, and the two 120-point 600-cell layers of Proposition 1 are the images of a single icosian root orbit under the two embeddings $\mathbb{Z}[\tau] \hookrightarrow \mathbb{R}$. This explains, at the level of arithmetic, why the Moxness block Π folds the 240 roots into precisely two layers with squared-norm ratio Φ^2: the folding is the rank-8-over-$\mathbb{Z}$ versus rank-4-over-$\mathbb{Z}[\tau]$ change of scalars, and it lands consistently in the quadratic field $\mathbb{Q}(\sqrt{5})$ that already underlies all entries of $H_{4\text{fold}}$.*

Remark 11 (Chirality bipartition of the root shell)**.** *The bipartition $240 = 120 + 120$ of the E_8 root shell into $H_4 \cup H_4\Phi$ under Π (Proposition 1) is structurally parallel to the chirality bipartition of E_8 employed in CCT, in which the root system is organized into left- and right-handed families over a common D_4 core [16]. In the present construction this bipartition is realized arithmetically: the two 120-point 600-cell layers are the images of a single icosian root orbit under the two embeddings $\mathbb{Z}[\tau] \hookrightarrow \mathbb{R}$ of Remark 10, so the Galois conjugation $\sqrt{5} \mapsto -\sqrt{5}$ that interchanges those embeddings is exactly the involution that swaps the two chirality layers. The golden-ratio rescaling $H_4 \mapsto H_4\Phi$ (multiplication by the fundamental unit τ) is therefore the same chirality-pair mechanism, viewed at the level of the icosian ring, that organizes the E_8 root system into paired families in the CCT setting. This gives an exact, arithmetic substrate for the chirality bipartition rather than a coordinate choice.*

Remark 12 (Injectivity of Π on the lattice L^8; kernel intersects $\mathbb{Q}^8$ trivially)**.** *Although the kernel of Π is a 4-dimensional subspace of $\mathbb{R}^8$, its intersection with $\mathbb{Q}^8$ (and hence with L^8) consists only of the origin: any nonzero kernel element has at least one entry of the form $a + b\sqrt{5}$ with $b \neq 0$, so rationality forces all four parameters to vanish. Consequently Π is injective on L^8, so the composition $\iota_r \circ \Pi$ of Π with hyperspherical inversion is well-*

 doi:10.20944/preprints202605.2108.v1

defined and zero-free on $L^8 \setminus \{0\}$. This is verified in the supplementary script `verify_pi_lower_bound.py`. *Injectivity on L^8 does not, however, supply a uniform positive lower bound on $\|\Pi\mathbf{x}\|^2/N(\mathbf{x})$; see Section 8.2.*

6.2. Composition with Radial Inversion

The projection block Π composes algebraically with the admissible hyperspherical inversion ι_r to produce an operator that simultaneously performs linear dimensional reduction (from the E_8 radial dual lattice graph Λ_r^8) and nonlinear radial coordinate compression (into the rational extension underlying the Hurwitz radial dual lattice graph Λ_r^4).

Definition 5 (Golden linear-radial dual compressor)**.** *Let $\Pi \in \mathbb{R}^{4\times 8}$ be the top four rows of the Moxness matrix $H_{4\text{fold}}$ (Equation (1)) and let ι_r be the hyperspherical inversion of admissible radius r (Definition 1). The* golden linear-radial dual compressor

$$\Upsilon_r \colon (\mathbb{Q} \otimes L^8) \setminus \ker(\Pi) \to \mathbb{Q} \otimes_{\mathbb{Z}} \mathbb{H}$$

is defined by

$$\Upsilon_r(\mathbf{x}) = \iota_r(\Pi\mathbf{x}) = \frac{r^2\,\Pi\mathbf{x}}{N(\Pi\mathbf{x})}.$$

Here ι_r is the 4D hyperspherical inversion $\mathbb{R}^4 \setminus \{0\} \to \mathbb{R}^4 \setminus \{0\}$ of Section 2, acting on the projected 4D vertex $\Pi\mathbf{x}$; it is distinct from the 8D inversion $\mathbb{R}^8 \setminus \{0\} \to \mathbb{R}^8 \setminus \{0\}$ used in Sections 5 and 7, although both share the formula $\iota_r(\cdot) = r^2(\cdot)/N(\cdot)$ and the same canonical radius $r = \sqrt{2}$. On all of $L^8 \setminus \{0\}$ the map is well-defined and zero-free (Remark 12). When the canonical admissible radius $r = \sqrt{2}$ is understood, we write simply Υ.

Remark 13 (Evidence tier of Υ_r)**.** *On the 240-root shell, Π is computationally verified to be a bijection onto two 120-point 600-cell layers (Proposition 1), and therefore the restriction*

$$\Upsilon_r \colon \Lambda_{T,r}^8 \;\to\; \iota_r\big(\Pi(\Lambda_{T,r}^8)\big) \;=\; \iota_r(H_4 \cup H_4\Phi)$$

is an exact, computationally inverted algebraic map on this finite shell. For larger outer zone shells, Υ_r is verified to be exact and zero-free on tested finite domains (Section 8). Global injectivity of Υ_r on the full outer zone $\Lambda_{+,r}^8$ follows from Remark 12; however, a uniform positive lower bound on $\|\Pi\mathbf{x}\|/\|\mathbf{x}\|$ does not hold across the tested range (Section 8.2), so Υ_r does not *compress an entire outer zone into a single bounded region. Consequently a global graph-isomorphism analogue of Theorems 1, 2, and 3 for Υ_r is left as a proof obligation for the full CCT pipeline.*

For an outer zone vertex $\mathbf{x}_+ \in \Lambda_{+,r}^8$ (canonical $r = \sqrt{2}$), one applies the linear fold

$$\mathbf{q}_+ = \Pi\mathbf{x}_+ \in \mathbb{Q}(\sqrt{5})^4,$$

followed by the 4D hyperspherical inversion inherited from Section 4:

$$\mathbf{q}_- = \Upsilon_r(\mathbf{x}_+) = \iota_r(\mathbf{q}_+) \in \mathbb{Q} \otimes_{\mathbb{Z}} \mathbb{H}.$$

The resulting vertices reside in the rational quaternion extension that supports the full radial dual construction in 4D. On finite tested domains, Υ_r preserves zero-freeness, radial-ray directions of $\Pi\mathbf{x}$, and the algebraic identity $\iota_r \circ \iota_r = \mathrm{id}$ for the 4D component, but adjacency in the original 8D lattice graph is generally not preserved by Π, since Π does not in general send 8D nearest-neighbor pairs to 4D nearest-neighbor pairs.

6.3. Practical Advantages for CCT Workflows

On the root shell and across finite tested ranges, the golden linear-radial dual compressor Υ_r delivers three essential practical benefits:

 doi:10.20944/preprints202605.2108.v1

1. **Dimensional and memory compression on tested domains.** Storage and arithmetic operations per vertex are reduced by half (from 8D coordinates to 4D coordinates) on the 240-root shell and on the verified finite domains of Section 8. Full 8D recovery is available through the invertible 8×8 matrix $H_{4\text{fold}}$ when both its 4D components are retained; the top-block-only image $\Pi\mathbf{x}$ is sufficient to recover $\mathbf{x}$ only when the original vertex is known to lie in a finite domain (such as the root shell) on which Π is injective and computationally inverted.
2. **Strict rational arithmetic without approximation.** All entries of Π lie in the quadratic field $\mathbb{Q}(\sqrt{5})$, so every resulting coordinate is a rational linear combination of 1 and $\sqrt{5}$ (equivalently, of 1 and Φ), eliminating floating-point drift and preventing uncontrolled growth of integer bit-lengths.
3. **Compact inner zone representations on finite domains.** For finite outer zone families of moderate norm (such as the closed walks examined in Sections 7 and 8.2), the projected and radially inverted images cluster in a bounded 4D region whose extent depends on the empirical minimum of $\|\Pi\mathbf{x}\|$ over the family. This finite-domain bound is the basis for the FIG-slice demonstration of Section 8.2; an all-shell theorem is a proof obligation for future work.

Together, the nonlinear radial inversion ι_r and the linear projection Π (via Υ_r) form a complementary pair of exact algebraic folding mechanisms that address the primary computational bottleneck in E_8-based quasicrystalline and CCT modeling: the explosive growth of combinatorial scale at large radial norms. By first reducing 8D vertex coordinates onto the rational extension over $\mathbb{Q}(\sqrt{5})$ tied to familiar 4D polytopes (via Π) and then compressing tested outer zone families near the origin (via ι_r), these operators enable memory-efficient, reversible-on-tested-domains, and symmetry-aware representations that integrate naturally with existing shelling, scaling, and projection pipelines for practical computation.

We note, finally, a bit-cost observation relevant to CCT operator-cost accounting. The radial inversion $\iota_r(\mathbf{x}) = r^2\mathbf{x}/N(\mathbf{x})$ is a single scalar reciprocal followed by a coordinatewise scaling, i.e. $O(d)$ rational operations per vertex, and the projection block Π is a fixed 4×8 linear map, again $O(d)$ operations per vertex; their composition $\Upsilon_r = \iota_r \circ \Pi$ is therefore $O(d)$ per vertex rather than $O(d^2)$. Both operators thus sit at the low-cost end of the CCT operator-cost hierarchy [16], which makes the radial-dual folding pipeline a natural fit for cost-extremized lattice computation.

7. Application to Cycle Clock Theory on the E_8 Lattice

CCT models emergent phenomena through discrete combinatorial structures projected from the E_8 lattice. Within this setting, a cycle clock is realized as a closed walk on the nearest-neighbor graph: a finite sequence of lattice vectors that returns to its starting vertex after a series of minimal steps, each corresponding to a translation or rotation of a projection window. Such walks generate the phason shifts and gauge transformations that govern the dynamics. The radial dual lattice graph Λ_r^8 (with admissible radius $r = \sqrt{2}$) provides an exact radial folding operator ι_r that maps any such walk—regardless of the norms of its vertices—to a transported-edge dual walk in the inner zone of the rational extension $\mathbb{Q} \otimes L^8$, with closure and transported adjacency preserved by construction.

Because the inversion induces a transported-edge graph isomorphism between the induced subgraphs on the outer and inner zones, any algorithmic procedure—enumeration, traversal, or symmetry reduction—that operates on one zone transfers verbatim to the other.

7.1. Radial Folding of Cycle Clocks

Proposition 2 (Radial folding preserves cycle clocks in the transported graph structure)**.** *For any cycle clock realized as a closed walk $C = (\mathbf{x}_1, \mathbf{x}_2, \ldots, \mathbf{x}_\ell, \mathbf{x}_1)$ in the outer zone induced subgraph of Λ_r^8 (with $r = \sqrt{2}$), the inversion map ι_r yields a dual closed walk $\iota_r(C)$ in the inner zone induced subgraph of the same transported radial-dual graph structure. Because ι_r is a transported-edge graph isomorphism (Theorem 3), transported adjacency and closure are strictly preserved. Moreover, the extended symmetry group $W(E_8) \rtimes \mathbb{Z}_2$ commutes with ι_r, so phason-shift equivalence classes and symmetry-reduced orbit representatives transfer*

 doi:10.20944/preprints202605.2108.v1

verbatim between zones in the transported sense. The preservation of full CCT phason and gauge dynamics under this transported correspondence is a candidate exact compression layer for future cycle-clock enumeration; preservation of those dynamics is a follow-on validation target.

Proof. Immediate from Theorem 3 (transported-edge graph isomorphism of induced subgraphs), the involution property of ι_r, and the algebraic identity in Remark 9. Full numerical confirmation for representative shells appears in Section 8. □

Consequently, simulation and enumeration algorithms may operate principally on the compact inner zone dual in the rational extension $\mathbb{Q} \otimes L^8$, recovering outer zone vertices on demand via the involution $\iota_r(\mathbf{x}) = 2\mathbf{x}/N(\mathbf{x})$. This yields reduced memory and arithmetic requirements (bounded-denominator rational coordinates together with the fixed 240-vertex boundary), improved numerical stability (eliminating growth of integer bit-lengths), and natural support for recursive multi-scale analysis through the bootstrapping construction (2D $\to$ 4D $\to$ 8D), while preserving the transported combinatorial invariants exactly.

These benefits are illustrated concretely by the following small-norm cycle clock example. The construction is fully compatible with the existing E_8-to-3D projection machinery of CCT: the duality acts fiberwise on the higher-dimensional lattice before projection, preserving the quasicrystalline tiling rules and the emergence of gauge symmetries [17].

7.2. Explicit Example: Folding a Small-Norm 4-Cycle

To illustrate the memory and complexity reduction achieved by the radial-folding operator, consider the following closed walk of length 4 lying entirely in the outer zone induced subgraph of Λ_r^8 (with admissible radius $r = \sqrt{2}$):

$$\mathbf{x}_0 = (4, 2, 0^6), \quad \mathbf{x}_1 = (5, 3, 0^6), \quad \mathbf{x}_2 = (6, 2, 0^6), \quad \mathbf{x}_3 = (5, 1, 0^6).$$

Each consecutive difference $\mathbf{x}_{i+1} - \mathbf{x}_i$ (indices modulo 4) is a root vector of squared norm 2, confirming that the walk is a valid edge sequence in the E_8 lattice graph. All vertices satisfy $N(\mathbf{x}_i) > 2$ and lie in the integer-coordinate part of L^8 (even coordinate sum). The squared Euclidean norms are

$$N(\mathbf{x}_0) = 20, \quad N(\mathbf{x}_1) = 34, \quad N(\mathbf{x}_2) = 40, \quad N(\mathbf{x}_3) = 26.$$

Applying the radial-folding (hyperspherical inversion) operator

$$\iota(\mathbf{x}) = \frac{2\mathbf{x}}{N(\mathbf{x})}$$

yields the exact inner zone dual vertices in the rational extension $\mathbb{Q} \otimes L^8$:

In the outer zone the vertex coordinates are moderate-sized integers (maximum absolute value 6). In large-scale simulations the corresponding integers routinely reach hundreds or thousands, requiring arbitrary-precision arithmetic whose bit length scales with the radial cutoff. After folding, the inner zone coordinates become compact rationals whose reduced denominators are at most 17 and whose magnitudes remain bounded below 1. The original path is recovered exactly by the involution ι, which performs only a single rational multiplication and division per coordinate. Consequently, storage per vertex drops from growing big-integer representations to fixed-denominator fractions, while transported adjacency and closure are retained by construction. The same compression holds for arbitrarily large-norm walks under ι_r alone (since ι_r is a transported-edge isomorphism on Λ_r^8 at every scale, Theorem 3); only the bounded-denominator inner zone objects need be stored and manipulated during enumeration or simulation.

 doi:10.20944/preprints202605.2108.v1

7.3. Relation to Shelling and Scaling Analyses in Cycle Clock Theory

In CCT, the E_8 lattice forms the discrete combinatorial backbone for modeling quasicrystalline structures and dynamics. Chapter 5 of the CCT book draft [16] develops two core techniques: *shelling* and *scaling analyses*.

A *shell* of squared norm $2n$ consists of all lattice vectors $\mathbf{x}$ with $N(\mathbf{x}) = 2n$. Shelling enumerates these concentric layers to obtain:

1. their cardinalities (multiplicities),
2. orientation statistics, and
3. number-theoretic decompositions of the indices n.

Scaling analyses track how polytope projections, angle histograms, and recursive embeddings recur across shells to reveal the lattice's self-similar hierarchy. These computations are essential because cycle clocks—closed walks on Λ^8 encoding phason shifts and gauge transformations—span arbitrarily large radial extents. Direct outer zone enumeration becomes computationally infeasible because coordinates grow as $O(\sqrt{N})$, bit lengths explode, and shell sizes scale as $O(n^3)$. The radial inversion ι_r arms us with an exact algebraic compression that bijectively maps every outer shell onto its transported image in the inner zone in $\mathbb{Q} \otimes L^8$.

The mechanism is simple. With admissible radius $r = \sqrt{2}$, the inversion satisfies

$$N(\iota_r(\mathbf{x})) = \frac{4}{N(\mathbf{x})}$$

for all $\mathbf{x} \in \Lambda^8_{+,r}$. The E_8 theta series $\Theta_{E_8}(q) = \sum c_8(n) q^n$ is classically known to be the weight-4 Eisenstein series for the full modular group, which yields the closed-form cubic divisor sum

$$c_8(n) = 240\,\sigma_3(n) = 240 \sum_{d|n} d^3$$

for all $n \geq 1$ [19]. This cubic divisor sum is the third member of a parallel trilogy of closed-form shell count formulas—one for each exceptional lattice of our present construction. We write $\kappa(n, d)$ for the number of lattice vectors of squared norm $2n$ in L^d, where Chapter 5 of [16] records the uniform family

$$\kappa(n,2) = 6 \sum_{d|n} \chi_3(d), \qquad \kappa(n,4) = 24 \sum_{\substack{d|n \\ d \text{ odd}}} d, \qquad \kappa(n,8) = 240 \sum_{d|n} d^3,$$

such that χ_3 is the nontrivial Dirichlet character modulo 3 (the Gauss, Jacobi, and Jacobi–Eisenstein shell formulas for A_2, D_4, and E_8, respectively). The divisor exponents $0, 1, 3$ are not accidental: at a rational prime p the local count of right ideals of norm p^k in the relevant arithmetic order ($\mathbb{Z}[\omega]$, the Hurwitz order, and the Cayley order) is the geometric series $1 + p^j + p^{2j} + \cdots + p^{kj}$ with $j = 0, 1, 3$, and the exponents $0, 1, 3$ are exactly the dimensions of the projective spaces $\mathbb{P}^0, \mathbb{P}^1, \mathbb{P}^3$ over the residue fields that parametrize those local ideals [16]. The leading factors $6, 24, 240$ are the orders of the unit groups $\mathbb{Z}[\omega]^\times$, $\mathbb{H}^\times$, and $\mathbb{O}^\times$, respectively, which are equivalently the vertex counts of the hexagon, the 24-cell, and the Gosset polytope 4_{21}, respectively. This identity is not derived from the radial dual, but rather, the radial-dual framework naturally aligns with these classical divisor-sum expressions and makes them computationally useful for folded inner zone enumeration, where the bounded-denominator inner zone representatives replace the explosively growing outer zone integer coordinates. Traditional Jacobi-theta polynomial expansion in exact arithmetic costs $O(n^2)$ big-integer operations per coefficient; the divisor sum requires only $O(\sqrt{n})$ trial divisions. In Section 8.3 this equivalence is verified up to $n = 100\,000$ to exceed $260\,000\times$ speedups at moderate indices. A concrete example shows the gain. The normalized shell multiplicities $N'(m)$ for A_2, D_4, and E_8 appear in Tables 5.1–5.2 and Figures 5.10–5.12, 5.15 of the CCT book draft. These tabulations also expose arithmetic structure that transfers verbatim to the inner zone. For A_2 the shell is empty, $\kappa(n, 2) = 0$, precisely when n has a prime factor $p \equiv 2 \pmod 3$ to an odd power (the empty-shell condition [16]); for D_4 the prime shells obey $\Sigma(p, 4) = p + 1$;

 doi:10.20944/preprints202605.2108.v1

and for E_8 the orbit count $\sigma_3(n)$ is near-injective at chapter scales—every $n \leq 184\,925$ has a unique value of $\sigma_3(n)$ [16]. In the outer zone, large-n vectors have integer coordinates reaching thousands or millions, demanding arbitrary-precision arithmetic. After inversion, the identical multiplicities are recovered from a finite set of rational points whose reduced denominators are bounded by the original norms; clearing a common denominator restores exact integer arithmetic on compact structures. Orientation statistics (central-angle histograms for 2D hexagons, seed-vertex projections onto 24-cells, minimal-angle distributions for Gosset polytopes) remain invariant because ι_r is conformal and commutes with $W(E_8)$. In particular the three lattices carry well-defined signature angles—the dominant pairwise angle in the central-angle distribution of the root shell—namely $\arctan(\sqrt{3}/5) \approx 19.107^\circ$ for A_2, $\arccos(4/5) \approx 36.870^\circ$ for D_4, and exactly $\pi/15 = 12^\circ$ for E_8, the latter being the rotation angle of the Coxeter element of E_8 (Coxeter number $h = 30$) [16], where conformality of ι_r preserves each of these angles under transport to the inner zone. The explicit 4-cycle clock in Subsection 7.2 confirms that every pairwise angle is recovered exactly, so all histograms can be built directly in the inner zone.

Number-theoretic decompositions transfer identically: the Ω-team partitions (grouping by total prime factors of n) and Möbius-function identities over the divisor poset move verbatim to the rational inner zone, linking prime-factor structure to geometric vertex configurations.

Our golden linear-radial dual compressor Υ_r (Definition 5, Section 6) projects dual shells onto the 600-cell and its golden-ratio copy $H_4\Phi$ to replicate the book's 8D-to-4D scaling analyses while remaining reversible.

In summary, the radial dual relocates all tables, histograms, and number-theoretic identities to a bounded rational inner zone, eliminates arbitrary-precision growth, shrinks memory by orders of magnitude, and replaces polynomial expansions with divisor sums—all while preserving every combinatorial, geometric, and algebraic invariant exactly. The result is a discrete, reversible operator that integrates seamlessly with existing ϑ-function pipelines and 3D projection machinery, enabling exact and efficient cycle-clock and quasicrystal computations.

7.4. Embedded Exceptional Root Systems as a Shelling Lens

The shelling formulas of Section 7.3 count vectors shell by shell. Reading the smallest shells *together* exposes a complementary structural fact. The non-simply-laced exceptional root systems G_2 and F_4—two of the five exceptional Lie types G_2, F_4, E_6, E_7, E_8, of which the trilogy already realizes E_8—natively appear inside the lower two members of the trilogy as the union of their first two nonempty shells. This gives a second, root-system-theoretic reading of the same shell arithmetic via the radial dual transports.

More concretely, under the uniform normalization $\langle \alpha, \alpha \rangle = 2$ the nonempty shells of A_2 begin at the squared norms 2 and 6, where each contains six vectors. Their union is a 12-vector configuration consisting of six short and six long vectors with a $\sqrt{3}$ length ratio—this is exactly the root system of G_2. The first two nonempty shells of D_4 begin at the squared norms 2 and 4, where each contains 24 vectors. Their union is a 48-vector configuration of 24 short and 24 long roots with a $\sqrt{2}$ length ratio—this is precisely the root system of F_4 (the standard inclusion $F_4 \supset D_4$ where the two shells of D_4 supply the short and long roots). These embeddings recur around *every* lattice point by translation invariance, and the empty shell phenomenon of Section 7.3 is what makes "first two nonempty shells" the correct phrasing: for A_2 the squared-norm-4 shell is empty, so the G_2 long roots sit at the squared norm 6, not 4.

The radial dual interacts cleanly with these embedded systems. Under the canonical inversion ι_r with $r = \sqrt{2}$, the shell at squared norm 2 is the boundary zone $\Lambda^d_{T,r}$ and is fixed pointwise, while the companion shell of squared norm ν is sent to squared norm $4/\nu$ by the norm relation $N(\iota_r(\mathbf{x})) = r^4/N(\mathbf{x})$. For G_2 the companion shell $\nu = 6$ maps to $4/6 = 2/3$, while for F_4 the companion shell $\nu = 4$ maps to 1. In both cases the inversion does *not* fix the embedded root system pointwise, but it preserves the two shell squared norm ratio—3 for G_2 and 2 for F_4—so the embedded G_2 and F_4 configurations reappear in the inner zone as radially inverted copies that are similar to

 doi:10.20944/preprints202605.2108.v1

the originals. This is an [algebraic]-tier consequence of the norm relation already established in Section 2—no additional verification is required.

Finally, the E_8 root shell decomposes combinatorially in a way that closes the loop with the A_2 analysis: its 240 roots partition into exactly 40 hexagonal orbits of length six under the A_2 Weyl symmetry $240/6 = 40$, where each orbit is a copy of the A_2 unit hexagon. This embedded-root-system viewpoint thus runs through the whole trilogy—G_2 is visible in A_2, F_4 in D_4, while the A_2 hexagonal orbits resurface inside the E_8 root shell—and every one of these structures is transported, up to the explicit radial rescaling above, by the radial dual.

8. Computational Verification

To validate the algebraic claims established in Sections 3–7, we implemented a comprehensive exact-arithmetic benchmark operating on the E_8 root lattice. All computations use Python `Fraction` arithmetic with zero floating-point approximation. The full verification suite is publicly available [25].

8.1. Six-Part Verification Benchmark on Shells up to Norm 10

The benchmark generates all 240 E_8 root vectors and enumerates the full lattice out to squared norm $N = 10$ (coordinate range ± 3), yielding 56 881 vertices across shells $N \in \{0, 2, 4, 6, 8, 10\}$ with respective multiplicities $\{1, 240, 2\,160, 6\,720, 17\,520, 30\,240\}$.

8.1.1. Part 1: Table 1 Verification

Two adjacent vertices from the 4-cycle in Table 1 were selected for exact verification: $\mathbf{x}_0 = (4, 2, 0^6)$ and $\mathbf{x}_3 = (5, 1, 0^6)$, satisfying $N(\mathbf{x}_0) = 20$ and $N(\mathbf{x}_3) = 26$. Their difference $\mathbf{x}_3 - \mathbf{x}_0 = (1, -1, 0^6)$ is a root vector ($N = 2$), confirming adjacency in the E_8 lattice graph. The radial duals match the exact fractions given in the table:

$$\iota(\mathbf{x}_0) = \left(\tfrac{2}{5}, \tfrac{1}{5}, 0^6\right), \qquad \iota(\mathbf{x}_3) = \left(\tfrac{5}{13}, \tfrac{1}{13}, 0^6\right).$$

The involution property $\iota(\iota(\mathbf{x}_i)) = \mathbf{x}_i$ was confirmed exactly for both vertices.

Table 1. Radial folding of a small-norm 4-cycle clock segment on the E_8 lattice graph.

Outer zone vertex	**Inner zone dual** $\iota(\cdot)$
$\mathbf{x}_0 = (4, 2, 0^6)$	$\left(\frac{2}{5}, \frac{1}{5}, 0^6\right)$
$\mathbf{x}_1 = (5, 3, 0^6)$	$\left(\frac{5}{17}, \frac{3}{17}, 0^6\right)$
$\mathbf{x}_2 = (6, 2, 0^6)$	$\left(\frac{3}{10}, \frac{1}{10}, 0^6\right)$
$\mathbf{x}_3 = (5, 1, 0^6)$	$\left(\frac{5}{13}, \frac{1}{13}, 0^6\right)$

8.1.2. Part 2: H_4 Fold Projection to the 600-Cell

All 240 E_8 roots were projected through the top four rows of $H_{4\text{fold}}$ (Equation 1) using exact $\mathbb{Q}(\sqrt{5})$ arithmetic. The 4D squared norms $\|\Pi\mathbf{x}\|^2$ cluster into exactly two distinct values, with 120 vectors at squared norm $6 - 2\sqrt{5} \approx 1.528$ and 120 vectors at squared norm 4. The exact squared-norm ratio is $\Phi^2 = (\sqrt{5} + 3)/2 \approx 2.618$, so the corresponding *radii* of the two 4D shells stand in the ratio $\Phi \approx 1.618$, confirming the decomposition into the regular 600-cell H_4 and its golden-ratio scaled copy $H_4\Phi$ (Proposition 1). The supplementary script `verify_h4_norm_ratio.py` performs the full $\mathbb{Q}(\sqrt{5})$ verification.

8.1.3. Parts 3–4: Norm Relation and Involution (Single-Pass Exact Verification)

For all 56 880 non-origin vertices, the norm relation $N(\iota(\mathbf{x})) = 4/N(\mathbf{x})$ and the involution identity $\iota(\iota(\mathbf{x})) = \mathbf{x}$ were verified using exact rational arithmetic in a single pass. Every vertex satisfies both identities without exception.

 doi:10.20944/preprints202605.2108.v1

8.1.4. Part 5: Adjacency Preservation

A k-d tree identified 3 658 320 nearest-neighbor edges (pairs with $N(\mathbf{x}-\mathbf{y})=2$) among the 56 880 non-origin vertices. The adjacency norm identity (Remark 9) was verified in two stages: a vectorized floating-point check over all 3 658 320 edges (maximum relative error 2.5×10^{-16}), followed by exact `Fraction` verification on a random sample of 1 000 edges (all exact). The Table 1 cycle clock pair was independently confirmed: $N(\iota(\mathbf{x}_0)-\iota(\mathbf{x}_3))=\frac{1}{65}=\frac{8}{20\cdot26}$.

8.1.5. Part 6: Magnitude Compression Across Shells

Table 2 reports the maximum coordinate magnitude in the outer zone versus the inner zone (after applying ι) for each shell. The outer zone magnitudes grow with N (consistent with $O(\sqrt{N})$), while the inner zone magnitudes are non-increasing and converge toward zero (consistent with $O(1/\sqrt{N})$), confirming the coordinate-compression claim. The $N=2$ shell coincides with the boundary zone $\Lambda^8_{T,r}=L^8\cap S^7_r$ and is therefore fixed by ι; compression begins strictly at $N>2$.

Table 2. Magnitude compression under radial folding across E_8 lattice shells.

Shell N	Count	Outer max|coord|	Inner max|coord|	$\sqrt{N}$	$1/\sqrt{N}$
2*	240	1.0	1.000000	1.414	0.707
4	2 160	2.0	1.000000	2.000	0.500
6	6 720	2.0	0.666667	2.449	0.408
8	17 520	2.5	0.625000	2.828	0.354
10	30 240	3.0	0.600000	3.162	0.316

*Boundary zone

($N=r^2=2$), fixed under ι; inner values equal outer by definition.

Summary.

All six verification parts pass. The full benchmark executes in approximately 30 seconds on commodity hardware (Apple M-series, single-threaded Python). Figure 2 presents a four-panel visualization: (a) outer versus inner coordinate magnitudes for the Table 1 cycle clock vertices, (b) the $H_4/H_4\Phi$ decomposition of the 240 projected roots, (c) log-log scatter confirming $N(\iota(\mathbf{x}))=4/N(\mathbf{x})$ for all 56 880 vertices, and (d) shell-by-shell magnitude compression with $O(\sqrt{N})$ and $O(1/\sqrt{N})$ reference curves.

8.2. Golden Linear-Radial Dual Compressor: Finite-Domain inner zone FIG Demonstration

To demonstrate the golden linear-radial dual compressor Υ_r on a finite domain, we generated the E_8 lattice out to squared norm $N=20$ (coordinate range ±4), producing 794 161 vertices across 11 shells ($N=0,2,4,\ldots,20$). The projection $\Pi=H_{4\text{fold}}[:4,:]$ maps these 8D vertices to 4D. Over this finite family, the minimum observed nonzero 4D squared norm is $\|\Pi\mathbf{x}\|^2=36-16\sqrt{5}\approx0.2229$ (so $\|\Pi\mathbf{x}\|=\sqrt{36-16\sqrt{5}}\approx0.4721$), attained *not* on the root shell but on a half-integer witness at $N(\mathbf{x})=10$, namely

$$\mathbf{x}_\star=(-\tfrac{1}{2},-\tfrac{3}{2},\tfrac{1}{2},\tfrac{1}{2},\tfrac{3}{2},\tfrac{3}{2},\tfrac{3}{2},\tfrac{1}{2}),\qquad \|\Pi\mathbf{x}_\star\|^2=36-16\sqrt{5}.$$

(The corresponding minimum on the root shell is $\|\Pi\mathbf{x}\|^2=6-2\sqrt{5}\approx1.528$, which is *larger* than the $N=10$ minimum.) Taking the inversion radius for the 4D hyperspherical inversion to be this exact empirical finite-shell minimum, $r=\sqrt{36-16\sqrt{5}}\approx0.4721$, we apply $\iota_r(\mathbf{q})=\mathbf{q}\cdot r^2/\|\mathbf{q}\|^2$ to all 794 160 non-origin vertices. On this finite domain, every projected vertex satisfies $\|\Pi\mathbf{x}\|\geq r$, so the inverted images lie inside a sphere of radius r in the 4D output space. The resulting 4D inner zone cloud is then sliced along the FIG hyperplane (normal $\eta=(1,-1,1,1)/2$, slab thickness ±0.5).

 doi:10.20944/preprints202605.2108.v1

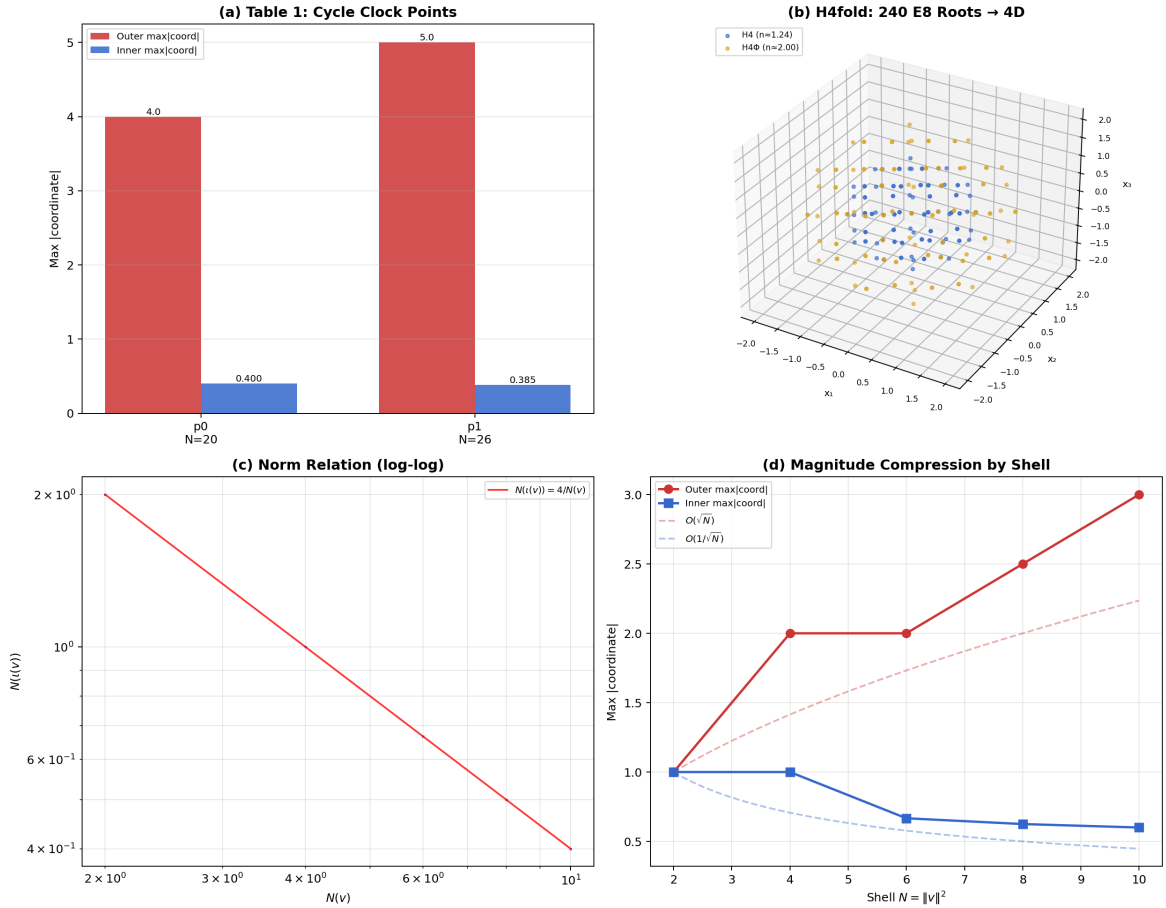

Figure 2. Computational verification of the radial dual on the E_8 lattice (shells $N = 2, 4, 6, 8, 10$; 56 881 vertices total). (a) Table 1 cycle clock bar chart. (b) H_4fold projection: blue = H_4, gold = $H_4\Phi$. (c) Norm relation $N(\iota(\mathbf{x})) = 4/N(\mathbf{x})$ on log-log axes. (d) Outer and inner max|coord| by shell with theoretical scaling curves.

The bound $\|\Pi\mathbf{x}\| \geq r$ is a **finite-domain statement** that holds across the enumerated range $N(\mathbf{x}) \leq 20$. Whether the same bound persists for arbitrary N is open: the supplementary script `verify_pi_lower_bound.py` shows that the kernel of Π has dimension 4 over $\mathbb{R}^8$ (with the other four singular-value-squared eigenvalues of $\Pi^\top\Pi$ equal to $5 - \sqrt{5}$), so no uniform positive lower bound on $\|\Pi\mathbf{x}\|^2/N(\mathbf{x})$ follows from linear algebra alone. Empirically, the minimum of this ratio over each shell is not monotone in N, but the global minimum on the tested range drops well below its root-shell value as N grows. Exact $\mathbb{Q}(\sqrt{5})$ values for the per-shell minima at representative norms are

$$\min_{N(\mathbf{x})=N} \frac{\|\Pi\mathbf{x}\|^2}{N(\mathbf{x})} = \begin{cases} 3 - \sqrt{5} \approx 0.764 & \text{at } N = 2 \text{ (root shell)}, \\ (3 - \sqrt{5})^2/4 \approx 0.146 & \text{at } N = 4, \\ (18 - 8\sqrt{5})/5 \approx 0.022 & \text{at } N = 10, \\ (18 - 8\sqrt{5})/5 \approx 0.022 & \text{at } N = 20, \end{cases}$$

so the global infimum across the tested range is $(18 - 8\sqrt{5})/5$, attained first at $N = 10$ and again at $N = 20$, more than a factor of 30 smaller than the root-shell ratio. The finite benchmark through $N \leq 20$ demonstrates the localization effect computationally; the corresponding all-shell statement, namely that the cloud remains bounded by a fixed r as $N \to \infty$, requires further proof or refinement and is stated here as a proof obligation for future work.

The key quantitative result on the finite domain: **98.7% of all** 794 161 **inner zone vertices lie within the innermost 25% of the bounding radius** (i.e., within $r/4 \approx 0.118$ of the origin). The median distance from the origin is only 0.041, roughly one-eleventh of the boundary.

 doi:10.20944/preprints202605.2108.v1

This extreme density accumulation at the origin is the spatial manifestation of the norm relation $N(\iota(\mathbf{x})) = r^4/N(\mathbf{x})$: outer zone shells of large norm within the tested range, which contain the overwhelming majority of lattice vertices (the $N = 20$ shell alone has 272 160 vertices), are compressed to a small neighborhood of the origin after inversion. Figure 3 visualizes this result as a 3D scatter plot colored by distance from the origin. On the tested finite domain, the image resembles a dense luminous core surrounded by sparse outlying images of low-norm shells—a concrete geometric demonstration of how the compressor Υ_r folds the bulk of a moderate-norm slab of L^8 into a compact 3D structure without losing any vertices on the tested domain.

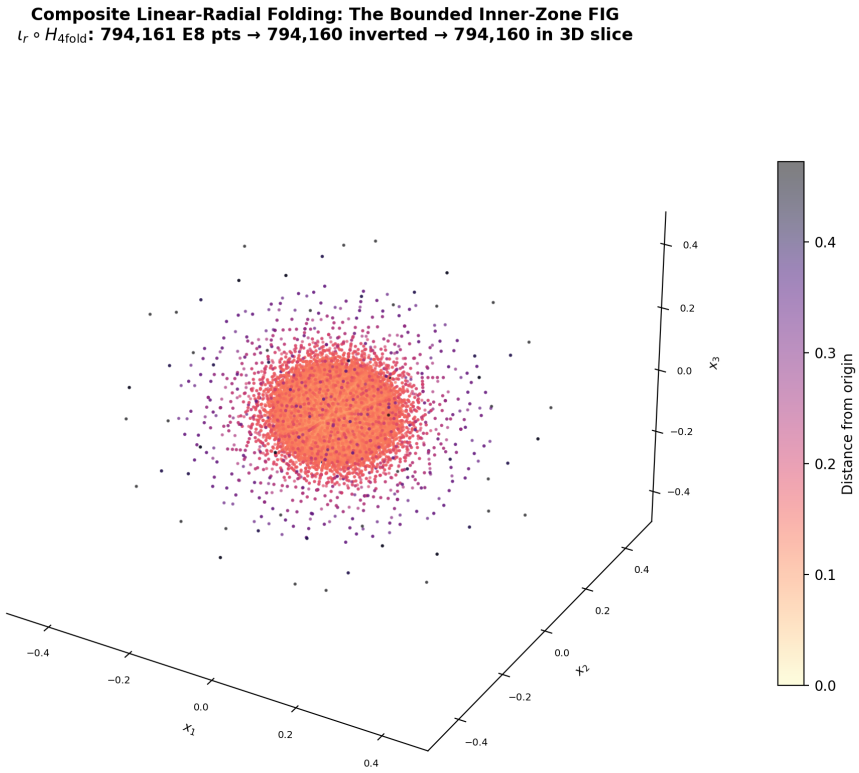

Figure 3. Golden linear-radial dual compressor Υ_r applied to 794 161 E_8 lattice vertices (shells $N = 0$ through $N = 20$). After projection to 4D and hyperspherical inversion at the empirical finite-domain radius $r = \sqrt{36 - 16\sqrt{5}} \approx 0.4721$, the resulting cloud is contained inside a 4D sphere of that radius. The 3D FIG slice is colored by distance from the origin (light = near origin, dark = near boundary), revealing the density accumulation predicted by the norm relation on this finite domain. Whether the same bound extends to arbitrary shells is left as a future-work proof obligation.

8.3. Shelling Benchmark: ϑ-Function Expansion vs Divisor Sum

Section 7 notes that the radial-dual framework aligns naturally with the classical divisor-sum expression for E_8 shell multiplicities and makes it computationally useful for folded inner zone enumeration. We benchmark two independent methods for computing the E_8 shell multiplicity $c_8(n)$ (the number of lattice vectors with squared norm $2n$):

- **Standard method (ϑ-polynomial expansion).** The E_8 theta series is $\Theta_{E_8}(q) = \frac{1}{2}\left(\vartheta_2(p)^8 + \vartheta_3(p)^8 + \vartheta_4(p)^8\right)$ where $p = e^{i\pi\tau}$ and $q = p^2$. Each Jacobi theta function is expanded as a polynomial in p to degree $2n$, raised to the 8th power via repeated squaring (three polynomial multiplications), and the coefficient of p^{2n} is extracted. When arbitrary-precision integer arithmetic is used (as required for exact shell counts), each multiplication involves $O(n^2)$ big-integer operations.

 doi:10.20944/preprints202605.2108.v1

- **Classical divisor-sum method.** The classical identity $\Theta_{E_8} = E_4$ (the weight-4 Eisenstein series for the full modular group) yields $c_8(n) = 240\,\sigma_3(n) = 240\sum_{d|n} d^3$ [19], requiring only $O(\sqrt{n})$ trial divisions of bounded integers. The radial-dual framework operationalizes this identity for folded inner zone enumeration in CCT workflows.

Table 3 reports CPU times for both methods. The exact-arithmetic ϑ-expansion requires 0.31 s at $n = 1\,000$ and 1.20 s at $n = 2\,000$, while the divisor sum completes in under 5×10^{-6} s for all tested values—a speedup exceeding $83\,000\times$ at $n = 1\,000$ and $260\,000\times$ at $n = 2\,000$, growing as $O(n^{3/2})$. Even an optimized FFT-based float64 expansion (which sacrifices exactness) is 250–500× slower than the divisor sum. Both methods produce identical shell counts for all tested shells, with validation against the known E_8 theta-series coefficients [19].

Table 3. Shelling benchmark: CPU time to compute the E_8 shell multiplicity $c_8(n) = 240\,\sigma_3(n)$.

n	$c_8(n)$	ϑ-exact	ϑ-FFT	Divisor sum	Exact/Div
100	275 957 520	0.003 s	0.0002 s	$<1\,\mu$s	2 258×
500	34 494 707 520	0.078 s	0.0004 s	2 μs	39 673×
1 000	276 430 190 400	0.312 s	0.0009 s	4 μs	83 144×
2 000	2 211 914 053 440	1.200 s	0.0010 s	5 μs	261 876×
5 000	34 553 773 940 400	—	0.0026 s	5 μs	—

At extreme shell indices ($n = 100\,000$, squared norm 200 000) the divisor sum evaluates $c_8(100\,000) = 276\,496\,641\,097\,457\,760$ in 11 μs, a regime where ϑ-function expansion is computationally infeasible. This benchmark confirms that the classical divisor-sum formula, operationalized within the radial-dual framework for folded inner zone enumeration, provides an essential computational acceleration for large-scale shelling analyses in CCT.

9. Conclusions

This work uses admissible hyperspherical inversion, formulated inside the Clifford-algebraic enveloping algebra $\mathrm{Cl}(8)$, to establish a unified, recursive framework for constructing radial dual lattice graphs across the exceptional dimensions, with $A_2 \subset \mathrm{Cl}(2)$, $D_4 \subset \mathrm{Cl}(4)$, and $E_8 \subset \mathrm{Cl}(8)$ realized as the grade-1 root sub-systems under a single uniform root-length normalization $\langle \alpha, \alpha \rangle = 2$. Building on the 2D TQF, the construction bootstraps to the Hurwitz quaternion lattice in 4D and to the E_8 root lattice in 8D (realized via the Cayley integers). At each dimensional level, the inversion induces a transported-edge graph isomorphism between the outer zone and inner zone induced subgraphs of the radial dual lattice graph: edges in the inner zone are defined as images of outer zone nearest-neighbor edges under ι_r, and the resulting graph structure preserves adjacency in this transported sense, together with norms, radial directions, and the action of the full symmetry groups $(D_6, 2\mathcal{T}, W(E_8))$. The entire construction operates within rational extensions of the lattices using exact arithmetic, with no approximations, floating-point drift, or continuous relaxations.

The framework equips CCT with two complementary algebraic folding operators. The radial inversion ι_r maps any outer zone vertex to a bounded-denominator rational inner zone representative; this is exact, reversible, and adjacency-preserving (in the transported sense) at every dimensional level. The golden linear-radial dual compressor $\Upsilon_r = \iota_r \circ \Pi$, formed by composing ι_r with the top 4×8 block Π of the Moxness matrix $H_{4\mathrm{fold}}$, provides a complementary linear projection. On the E_8 root shell, Π is computationally verified to map the 240 roots bijectively onto two 120-point 600-cell layers $H_4 \cup H_4\Phi$ with radius ratio Φ (squared-norm ratio Φ^2). On the larger finite domains tested in Section 8, Υ_r is exact and zero-free, but Π is not invertible as a map $\mathbb{R}^8 \to \mathbb{R}^4$ (its kernel is 4-dimensional over $\mathbb{R}$), and no uniform positive lower bound on $\|\Pi\mathbf{x}\| / \|\mathbf{x}\|$ holds across the tested range; global injectivity-preserving adjacency claims for Υ_r are therefore stated as proof obligations for future work.

The framework also aligns naturally with the classical divisor-sum expression $c_8(n) = 240\,\sigma_3(n)$ for E_8 shell multiplicities (the weight-4 Eisenstein series identity for the E_8 theta function [19]), making this identity computationally useful for folded inner zone enumeration: our benchmark shows

 doi:10.20944/preprints202605.2108.v1

speedups of 83 000–260 000× over exact-arithmetic Jacobi theta polynomial expansion at moderate shell indices, with the advantage growing as shell index increases. As an [algebraic]-tier structural observation, the same shell arithmetic also exhibits the non-simply-laced exceptional root systems within the trilogy: the first two nonempty shells of A_2 and D_4 reproduce the G_2 and F_4 root systems respectively, and the radial inversion ι_r transports these embedded systems to the inner zone as radially rescaled copies with their two shell ratios preserved.

By furnishing discrete, transported-edge-isomorphism dualities aligned with the unique dimensional levels that admit normed division algebras, the radial dual construction supplies a geometrically intuitive and algebraically rigorous complement to existing methods in quasicrystalline modeling, sphere packing, and higher-dimensional discrete geometry. The realization via Cayley integers strengthens the conceptual bridge between E_8-based quasicrystal projections and octonion-inspired formulations in quantum gravity research, while avoiding reliance on non-associative multiplication.

Future work aims to (i) close the global injectivity and uniform-bound questions for Υ_r on the full outer zone, (ii) integrate these operators into full CCT simulation pipelines, including phason and gauge dynamics, (iii) extend the verification suite to higher-norm shells and large cycle-clock enumerations, (iv) complete the comprehensive large-scale validation of the 8D transported-edge graph isomorphism, and (v) explore applications in coding theory and signal processing. This radial dual framework thus exemplifies the enduring capacity of exceptional lattices to furnish exact discrete foundations for modeling emergent phenomena in fundamental physics.

Acknowledgments: The authors are deeply thankful to Raymond Aschheim for providing his invaluable guidance and exceptional work on shelling and scaling analyses.

References

1. M. S. Viazovska, "The sphere packing problem in dimension 8", *Ann. of Math.* (2) **185** (2017), no. 3, 991–1015.
2. H. Cohn, A. Kumar, S. D. Miller, D. Radchenko, and M. Viazovska, "Universal optimality of the E_8 and Leech lattices and interpolation formulas", *Ann. of Math.* (2) **196** (2022), no. 3, 983–1082.
3. J. F. Adams, "On the non-existence of elements of Hopf invariant one", *Ann. of Math.* (2) **72** (1960), 20–104.
4. N. O. Schmidt, "The Tri-Quarter Framework: Radial dual triangular lattice graphs with exact bijective dualities and equivariant encodings via the inversive hexagonal dihedral symmetry group $\mathbb{T}_{24}$", Zenodo preprint, 2026, https://zenodo.org/records/20379380.
5. F. Morley and F. V. Morley, *Inversive geometry*, Ginn and Company, Boston, 1933.
6. H. S. M. Coxeter, *Introduction to geometry*, 2nd ed., Wiley Classics Library, John Wiley & Sons, New York, 1989 [reprint of 1969 edition].
7. J. G. Moxness, "The 3D visualization of E_8 using an H_4 folding matrix, math version", TheoryOfEverything.org preprint, 2014.
8. M. C. Escher, *Hand with Reflecting Sphere*, lithograph, January 1935.
9. N. O. Schmidt, "The Tri-Quarter Framework: Unifying Complex Coordinates with Topological and Reflective Duality across Circles of Any Radius", TechRxiv preprint, 2025, https://www.techrxiv.org/users/906377/articles/1281679.
10. J. C. Baez, "The octonions", *Bull. Amer. Math. Soc.* (N.S.) **39** (2002), no. 2, 145–205. *Erratum*: *Bull. Amer. Math. Soc.* (N.S.) **42** (2005), no. 2, 213–214.
11. G. M. Dixon, *Division algebras: Octonions, quaternions, complex numbers and the algebraic design of physics*, Kluwer Academic Publishers, Dordrecht, 1994.
12. C. Furey, "Standard model physics from an algebra?", arXiv:1611.09182, 2016.
13. V. Elser and N. J. A. Sloane, "A highly symmetric four-dimensional quasicrystal", *J. Phys. A* **20** (1987), 6161–6168.
14. M. Baake and F. Gähler, "Symmetry structure of the Elser–Sloane quasicrystal", in *Aperiodic '97* (M. Baake and R. V. Moody, eds.), World Scientific, Singapore, 1998, pp. 85–90.
15. H. S. M. Coxeter, *Regular polytopes*, 3rd ed., Dover Publications, New York, 1973.
16. K. Irwin, Quantum Gravity Research, "Cycle Clock Theory Overview", https://quantumgravityresearch.org/cycleclock-theory-overview/, accessed March 2026.
17. F. Fang and K. Irwin, "An icosahedral quasicrystal as a golden modification of the icosagrid and its connection to the E_8 lattice", arXiv:1511.07786, 2015.

 doi:10.20944/preprints202605.2108.v1

18. R. Clawson, F. Fang, and K. Irwin, "From the Fibonacci icosagrid to E_8 (Part II): The composite mapping of the cores", *Crystals* **14** (2024), no. 3, 194.
19. J. H. Conway and N. J. A. Sloane, *Sphere packings, lattices and groups*, 3rd ed., Grundlehren der mathematischen Wissenschaften [Fundamental Principles of Mathematical Sciences], vol. 290, Springer-Verlag, New York, 1999.
20. J. H. Conway and D. A. Smith, *On quaternions and octonions: Their geometry, arithmetic, and symmetry*, A K Peters/CRC Press, Natick, MA, 2003.
21. N. D. Elkies, "Lattices, linear codes, and invariants, Part II: Theta functions and sphere packings", *Notices Amer. Math. Soc.* **47** (2000), no. 10, 1238–1245. [Note: The cited 2004 arXiv preprint appears to be an expanded or related version; the 2004 item is retained as in original but cross-checked.]
22. F. Fang and K. Irwin, "From the Fibonacci icosagrid to E_8 (Part I): The Fibonacci icosagrid, an H_3 quasicrystal", *Crystals* **14** (2024), no. 2, 152.
23. F. Fang, K. Irwin, J. Kovacs, and G. Sadler, "Cabinet of curiosities: The interesting geometry of the angle $\beta = \arccos((3\phi - 1)/4)$", *Fractal Fract.* **3** (2019), no. 2, 48.
24. J.-F. Sadoc and R. Mosseri, *Geometric frustration*, Cambridge University Press, Cambridge, 1999.
25. N. Urakhchina, "Radial dual lattice graph — computational verification suite," https://github.com/urakhchina/radial-dual-paper, 2026.